State-Specific Study of Air in the Expansion Tunnel Nozzle and Test Section

Sangdi Gu[*], Jiaao Hao[†] and Chih-yung Wen[‡]

The Hong Kong Polytechnic University, Kowloon, Hong Kong

Thermochemical nonequilibrium in expansion tunnel nozzles is investigated numerically using a state-to-state description in one-dimension for representative air conditions. Limiting the multi-quantum jumps of VVT transitions to 3 in both N_2 and O_2 can accurately simulate the nonequilibrium nozzle flow. The reduction of VVT transitions to VT transitions works well. State-to-state modelling of an actual expansion tunnel nozzle condition yielded agreement with the measured static pressure. A study on the influence of different thermochemical excitation in the freestream at the test section shows that the post-shock radiation emissions can differ by more than 50 %. However, the non-Boltzmann distributions in the freestream has no influence. An evaluation of the discrepancy between the two-temperature and state-to-state models shows that the former generally predicts a faster thermochemical relaxation. Furthermore, the state-to-state results indicate that, in general, the molecular species all have a different vibrational temperature.

Nomenclature

A	=	nozzle cross-sectional area
AB, CD	=	molecular species
A^s, B^s	=	atomic species
c	=	mass fraction
E	=	level energy
e_v	=	specific vibrational energy

[*] Research Assistant Professor, Department of Aeronautical and Aviation Engineering. sangdi.gu@polyu.edu.hk.
[†] Assistant Professor, Department of Aeronautical and Aviation Engineering. jiaao.hao@polyu.edu.hk. Member AIAA.
[‡] Chair Professor and Department Head, Department of Aeronautical and Aviation Engineering. cywen@polyu.edu.hk. Associate Fellow AIAA.

f	=	final vibrational quantum number
h_0	=	total specific enthalpy
i	=	initial vibrational quantum number
k	=	Reaction rate coefficient
k_B	=	Boltzmann's constant
M	=	collision partner in a reaction
$\mathcal{M}$	=	molar mass
P	=	probability
p	=	pressure
T	=	translational temperature
T_v	=	average vibrational temperature
u	=	velocity
$\dot{w}_\iota$	=	mass production rate
X	=	molar concentration
x	=	position along flow axis
ρ	=	mass density
$\tau_{AB\text{-}M}$	=	vibrational relaxation time

Subscripts

1	=	molecule 1 of a vibration–vibration–translation reaction
2	=	molecule 2 of a vibration–vibration–translation reaction
A^s, B^s	=	atomic species
AB, CD	=	diatomic species
EX	=	exchange reaction
i	=	species index
$inlet$	=	nozzle inlet
max	=	maximum vibrational level
v	=	vibrational level

Superscripts

eq   =   equilibrium

I. Introduction

Experimental hypersonics work is crucial for the development of hypersonic technology. Two types of wind tunnels used to facilitate this research is the expansion tunnel [1], and the nonreflecting shock tunnel [2]. Both types of wind tunnels are suitable of generating very high velocity test conditions (> 8 km/s) as they avoid stagnating the test gas, unlike in many of the other configurations [3]. As a result, the nozzles used in these two facilities are purely diverging nozzles, instead of the more common converging-diverging nozzles. Also, because these two facilities have shorter test times, the purely diverging nozzles have smaller exit area ratios as the test model size is limited by the test time due to the required flow establishment time [3]. Hence, although some studies already exist for high-enthalpy converging-diverging nozzles [4, 5], the characteristic differences between these nozzles and the purely diverging nozzles call for a separate dedicated study on the later. This is addressed in the current paper, focusing particularly on the expansion tunnel nozzle due to the popularity of this facility compared to that of the nonreflecting shock tunnel.

Fig. 1 presents the schematic of a conventional expansion tunnel along with the position-time (x-t) diagram showing the longitudinal wave processes which occur during the flow cycle. Upon rupture of the diaphragm (primary) separating the driver section and the shock tube (driven section), the driver gas (usually high pressure and high temperature helium) generates a propagating normal shock in the shock tube which is filled with the test gas. This normal shock heats the test gas and then breaks a very weak secondary diaphragm when it reaches the end of the shock tube. As the secondary diaphragm is very weak, a reflected shock is not formed and the test gas does not get stagnated. A one-dimensional centered unsteady expansion forms after the rupture of the secondary diaphragm. The shock heated test gas, which is already supersonic, travels through this unsteady expansion as it flows through the acceleration tube (which has the same cross-sectional area as the shock tube), further increasing its velocity. Finally, the test gas, upon reaching the end of the acceleration tube, goes through a further expansion in the nozzle. A steady nozzle flow is generated in the time interval between the contact surface and wave tail, as shown in Fig. 1. As the flow entering the

nozzle is already supersonic, the nozzle is a purely diverging one (no converging section). The reader is referred to Ref. [1, 3, 6-10] for more details on the expansion tunnel facility.
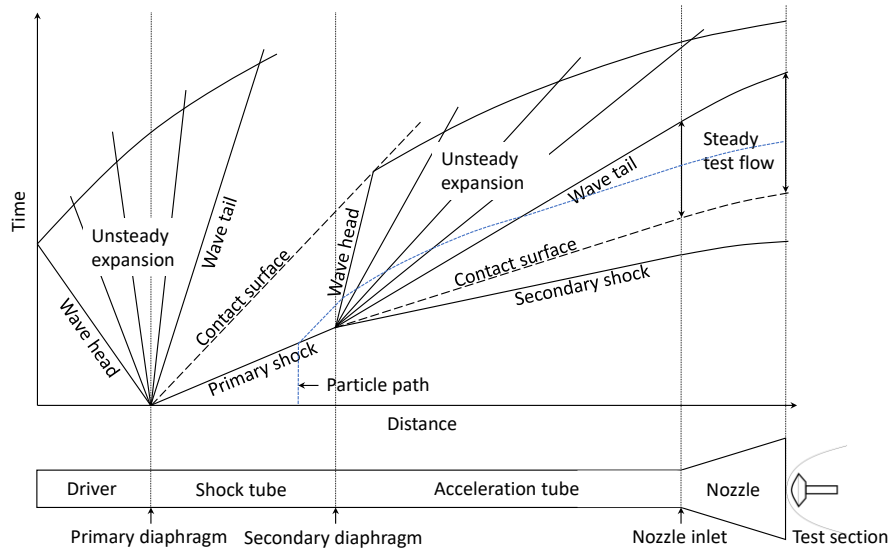

Fig. 1. The expansion tunnel and corresponding x-t diagram.

Some work has been done on modelling the flow cycle of expansion tunnels through detailed Navier-Stokes simulations using low fidelity thermochemical models – perfect gas, thermochemical equilibrium, and two-temperature models [11-13]. However, accurately characterizing the degree of thermochemical excitation in the experimental freestream is critical for the correct interpretation of experimental data for blunt and slender body studies as well as scramjet studies, and this concept is well documented in literature [4, 14-19]. High fidelity state-to-state (StS) thermochemical nonequilibrium models do exist, though their applications have mainly focused on shock waves and converging-diverging nozzle flows where excellent work has been done [20-26]. Though, as mentioned earlier, converging-diverging nozzle flows are not relevant to the expansion tunnel. Thus, there is considerable interest in applying StS models to simulate the nonequilibrium flows more relevant to the expansion tunnel. This paper addresses this interest by using a vibrational StS model to describe the thermochemical nonequilibrium in the expansion tunnel nozzle flow.

As mentioned earlier, and shown in Fig. 1, the test flow which enters the nozzle is processed earlier by a one-dimensional centered unsteady expansion. The qualitative aspects of this unsteady expansion are shown in Fig. 2. The flow near the fan center is close to the frozen limit while the flow further away is close to the thermochemical equilibrium limit. The actual quantitative structure of the expansion fan would depend on the flow condition, and the length and time scales involved. Subsequently, this would decide whether the flow entering the nozzle is in equilibrium

or nonequilibrium. While no systematic parametric study is reported in literature, existing experimental [7, 10, 27-32] and numerical [33-35] results indicate that the flow entering the nozzle is at or near thermochemical equilibrium at given operating conditions. At present, due to the lack of more rigorous and dedicated studies on the unsteady expansion process in the expansion tunnel, an equilibrium nozzle inlet condition is often assumed by the expansion tunnel community [9, 13, 36-40]. In fact, the contours of existing expansion tunnel nozzles have been designed assuming thermochemical equilibrium at the inlet [12, 41, 42]. Subsequent testing yielded good results, justifying this assumption as being at least reasonable. Thus, the nozzle inlet condition used throughout this paper is modelled as being in thermochemical equilibrium. All equilibrium calculations described in this work are made using Cantera [43].
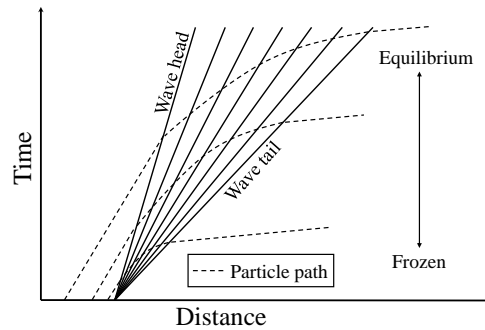

Fig. 2. A one-dimensional centered unsteady expansion fan shown in a x-t diagram.

In this paper, to assess the possibility of reduced order modelling, a study is performed to examine the influence of multi-quantum VVT transitions and the validity of simplifying VVT transitions to VT transitions. Then, state-specific modelling of an actual expansion tunnel nozzle condition is conducted. Comparisons are made with the perfect gas, thermochemical equilibrium, and two-temperature models, as well as experimental data. After that, the influence of different thermochemical excitations in the freestream is assessed for the flow behind a normal shock at the expansion tunnel test section (nozzle exit). Finally, an in-depth comparison between the StS model and the two-temperature model is carried out for a range of expansion tunnel nozzle operating conditions.

II. The Numerical Model

Due to the computational cost, coupling of a full StS model - with unrestricted multi-quantum transitions for all the VVT and VT reactions - to a multi-dimensional flow solver is currently impractical for an air mixture and, thus, the reacting nozzle flow in this work is modelled based on the quasi-one-dimensional steady Euler equations [44-47],

$$
\begin{aligned}
d\rho uA &= 0 \\
dp + \rho u\, du &= 0 \\
dh_0 &= 0 \\
dc_i - \frac{\dot{w}_i}{\rho u} dx &= 0
\end{aligned}
\tag{1}
$$

Though, it is acknowledged that nozzle flows can be multi-dimensional, as shown in Ref. [24, 26].

In the StS model, each vibrational state is considered a pseudo-species. The reaction processes considered in this study include $AB(i_1) + CD(i_2) \rightarrow AB(f_1) + CD(f_2)$ VVT transitions (molecule-molecule), $AB(i_1) + M \in \{$atoms or molecules$\} \rightarrow AB(f_1) + M$ VT transitions, $AB(i_1) + M \in \{$atoms or molecules$\} \rightarrow A^s + B^s + M$ vibration-dissociation (VD) reactions, and $AB(i_1) + O/N \leftrightarrow NO(f) + N/O$ exchange reactions. Consider a molecular species $AB \in \{N_2, O_2\}$ at a vibrational level i_1, the resulting species production rate can be written generally as [4, 48-50],

$$
\dot{w}_{AB(i_1)} = \mathcal{M}_{AB} \left[\left\{ \frac{\partial [AB(i_1)]}{\partial t} \right\}_{VVT} + \left\{ \frac{\partial [AB(i_1)]}{\partial t} \right\}_{VT} + \left\{ \frac{\partial [AB(i_1)]}{\partial t} \right\}_{VD} + \left\{ \frac{\partial [AB(i_1)]}{\partial t} \right\}_{EX} \right]
\tag{2}
$$

where

$$
\left\{ \frac{\partial [AB(i_1)]}{\partial t} \right\}_{VVT} = \sum_{i_2=0}^{i_{2,max}} \sum_{\substack{f_1=0 \\ f_1 \neq i_1}}^{f_{1,max}} \sum_{f_2=0}^{f_{2,max}} k_{VVT}(f_1, f_2 \rightarrow i_1, i_2) X_{f_1} X_{f_2} - k_{VVT}(i_1, i_2 \rightarrow f_1, f_2) X_{i_1} X_{i_2}
\tag{3}
$$

for the molecule-molecule interactions,

$$
\left\{ \frac{\partial [AB(i_1)]}{\partial t} \right\}_{VT} = \sum_{M} \sum_{\substack{f_1=0 \\ f_1 \neq i_1}}^{f_{1,max}} k_{VT}(f_1, M \rightarrow i_1, M) X_{f_1} X_M - k_{VT}(i_1, M \rightarrow f_1, M) X_{i_1} X_M
\tag{4}
$$

for the molecule-atom interactions and the molecule-molecule interactions where VVT reactions are not considered,

$$
\left\{ \frac{\partial [AB(i_1)]}{\partial t} \right\}_{VD} = \sum_{M} k_{VD}(A^s, B^s, M \rightarrow i_1, M) X_{A^s} X_{B^s} X_M - k_{VD}(i_1, M \rightarrow A^s, B^s, M) X_{i_1} X_M
\tag{5}
$$

for the dissociation/recombination reactions, and

$$
\left\{ \frac{\partial [AB(i_1)]}{\partial t} \right\}_{EX} = \sum_{f=0}^{f_{max}} k_{EX}(NO(f), N/O \rightarrow i_1, O/N) X_{NO(f)} X_{N/O} - k_{EX}(i_1, O/N \rightarrow NO(f), N/O) X_{i_1} X_{O/N}
\tag{6}
$$

for the NO exchange reactions. From these, one can easily derive the species production rate for N, O and $NO(i_1)$.

The energies of the vibrational levels for N_2, O_2 and NO used in this work are obtained from the STELLAR database [51], and they are determined by solving the radial Schrödinger equation with potential curves obtained from the Rydberg-Klynning-Rees method [52]. There are 61 bound levels for N_2, 46 for O_2, and 48 for NO. For all reactions,

the backward (AB(i_1) deexcitation, recombination, and NO destruction) reaction rates are computed from detailed balancing. The current work considers five major species – N_2, O_2 N, O and NO – and ionization is not considered. Additionally, only the ground electronic state is considered for all species.

The VVT and VT reactions considered in the current work are listed in Table 1. Reactions 1-3 are the VVT reactions with rates generated in a previous work by the current authors [53] using the Forced Harmonic Oscillator (FHO) theory [54, 55]. Comparisons with quasi-classical trajectory (QCT) and semi-classical (SC) calculations as well as experimental measurements were made, and varying degrees of agreements were observed - ranging from within 10 % to within an order of magnitude, depending on the temperature [53]. The remaining FHO rates in this table – reactions 4 and 5 – are obtained from the STELLAR database [56]. A comparison of these two rates with QCT and experimental rates was carried out by Ref. [57], and varying degrees of agreements were observed - ranging from within 10 % to within two orders of magnitude, depending on the temperature. Reactions 7 and 8 are the VT reaction of N_2 and O_2 colliding with N and O respectively for which the rates are obtained from QCT calculations [58, 59]. No state-specific rates are available for reactions 6 and 9 - 12, thus, the classic Landau-Teller (LT) model in StS form is applied, derived by Ref. [60],

$$k_{VT}(i_1, M \rightarrow f_1, M) = \frac{1}{X_M} \left(\frac{c_{AB(f_1)}}{c_{AB}} \right)^{eq} \frac{1}{\tau_{AB-M}} \tag{7}$$

where X_M is the molar concentration of the collision partner, c_{AB} is the mass fraction of $AB \in \{N_2, O_2, NO\}$, $c_{AB(f_1)}$ is the mass fraction of the pseudo-species $AB(f_1)$. The 'eq' superscript refers to the thermal equilibrium state. The vibrational relaxation time, $\tau_{AB\text{-}M}$, is calculated according to Millikan and White [61] with Park's high temperature correction [62].

Table 1.   Inelastic reactions considered in this work, where $M \in \{NO, O, N\}$.

No.	Reaction	Model	Ref.
1	$N_2(i_1) + N_2(i_2) \leftrightarrow N_2(f_1) + N_2(f_2)$	FHO	[53]
2	$O_2(i_1) + O_2(i_2) \leftrightarrow O_2(f_1) + O_2(f_2)$	FHO	[53]
3	$O_2(i_1) + N_2(i_2) \leftrightarrow O_2(f_1) + N_2(f_2)$	FHO	[53]
4	$NO(i) + N_2 \leftrightarrow NO(f) + N_2$	FHO	[56]
5	$NO(i) + O_2 \leftrightarrow NO(f) + O_2$	FHO	[56]
6	$NO(i) + M \leftrightarrow NO(f) + M$	LT	[60, 62]
7	$N_2(i) + N \leftrightarrow N_2(f) + N$	QCT	[58]
8	$O_2(i) + O \leftrightarrow O_2(f) + O$	QCT	[59]
9	$N_2(i) + O \leftrightarrow N_2(f) + O$	LT	[60, 62]
10	$O_2(i) + N \leftrightarrow O_2(f) + N$	LT	[60, 62]
11	$N_2(i) + NO \leftrightarrow N_2(f) + NO$	LT	[60, 62]
12	$O_2(i) + NO \leftrightarrow O_2(f) + NO$	LT	[60, 62]

Table 2. **Dissociation/recombination and exchange reactions considered in this work, where M $\in$ {NO, O, N}.**

No.	Reaction	Model	Ref.
1	$N_2(i) + N_2 \leftrightarrow 2N + N_2$	FHO	[56]
2	$O_2(i) + O_2 \leftrightarrow 2O + O_2$	FHO	[56]
3	$N_2(i) + O_2 \leftrightarrow 2N + O_2$	FHO	[56]
4	$O_2(i) + N_2 \leftrightarrow 2O + N_2$	FHO	[56]
5	$N_2(i) + N \leftrightarrow 3N$	QCT	[58]
6	$O_2(i) + O \leftrightarrow 3O$	QCT	[59]
7	$N_2(i) + O \leftrightarrow 2N + O$	Reaction 5	[62]
8	$O_2(i) + N \leftrightarrow 2O + N$	Reaction 6	[62]
9	$N_2(i) + NO \leftrightarrow 2N + NO$	Reaction 1	[62]
10	$O_2(i) + NO \leftrightarrow 2O + NO$	Reaction 4	[62]
11	$NO(i) + N_2 \leftrightarrow N + O + N_2$	FHO	[56]
12	$NO(i) + O_2 \leftrightarrow N + O + O_2$	FHO	[56]
13	$NO(i) + M \leftrightarrow N + O + M$	(Reaction 11) x 20	[62]
14	$N_2(i) + O \leftrightarrow NO(f) + N$	QCT	[63]
15	$O_2(i) + N \leftrightarrow NO(f) + O$	QCT	[64]

The dissociation and exchange reactions considered in this work are listed in Table 2. All FHO dissociation rates in this table are obtained from the STELLAR database [52, 56]. For reactions 1 and 2 in this table, comparisons of the FHO rates with QCT calculations and experimental measurements were made by Ref. [4, 51, 52, 65]; agreements within 10 % to within two orders of magnitude were observed, depending on the temperature. For reactions 3 and 4 in this table, comparisons of the FHO rates with experimental measurements were made by Ref. [4]; agreements within 10 % to within two orders of magnitude were observed, depending on the temperature. Reactions 5 and 6 are the dissociation reaction of N_2 and O_2 colliding with N and O respectively for which the rates are obtained from QCT calculations [58, 59]. For reactions 14 and 15, the state-specific NO exchange reaction rates are obtained from the QCT calculation of Ref. [63, 64], which have been rigorously assessed with respect to experimental and other theoretical results [60, 66-68]. Order of magnitude agreements were observed, though the present rates were shown to be consistently a bit slower than some of the other results [66-68]. For the dissociation reactions where no state-specific rates are available, the concept of third body efficiencies is applied using the efficiencies given by Park [62], which is a common approximation [67].

III. On the reduction of VVT transitions

A. Influence of multi-quantum transitions in VVT transitions

State-to-state (StS) modelling, particularly ones where VVT transitions are modeled, generally involves huge amounts of reactions. This is a computational issue, with the bottleneck being the evaluation of the master equation

[69]. As a result, its use in multi-dimensional Navier-Stokes solvers is prohibitively expensive. In general, the probability of a transition decreases with increasing magnitude of the quantum jump involved in the transition. So, the transition rates between two quantum levels very far apart may be so small as to be considered negligible. Therefore, it is of interest to investigate this for VVT transitions for the possibility of reduced order modelling and improving computational time.

Table 3. Numerical test condition.

Inlet velocity, km/s	Inlet static pressure, kPa,	Inlet static temperature, K	Conical nozzle half-angle, deg	Inlet radius, m
5.0	10	3000	35	0.1

Table 4. Level based multi-quantum transition cases

Case	$\Delta v_{max,O2}$	$\Delta v_{max,N2}$	No. of VVT transitions
L1	All	35	2.0×10^7
L2	All	25	1.5×10^7
L3	All	15	1.0×10^7
L4	All	5	6×10^6
L5	35	All	2.5×10^7
L6	25	All	2.3×10^7
L7	15	All	2.0×10^7
L8	5	All	1.6×10^7
L9	All	All	2.6×10^7
L10	1	1	6.7×10^4

The numerical test condition used for this study is shown in Table 3, and it is representative of an expansion tunnel nozzle inlet condition. A conical nozzle with a 35° half-angle is used as the geometry. As the VVT reactions dominate the total number of reactions, multi-quantum restrictions are applied to these reactions. The multi-quantum transition rules tested are shown in Table 4 along with the corresponding number of VVT transitions. Cases 'L1' to 'L4' tests the influence of N_2 multi-quantum transitions while cases 'L5' to 'L8' tests the influence of O_2 multi-quantum transitions. Additionally, case 'L9' considers all possible quantum transitions while case 'L10' considers only single-quantum transitions.
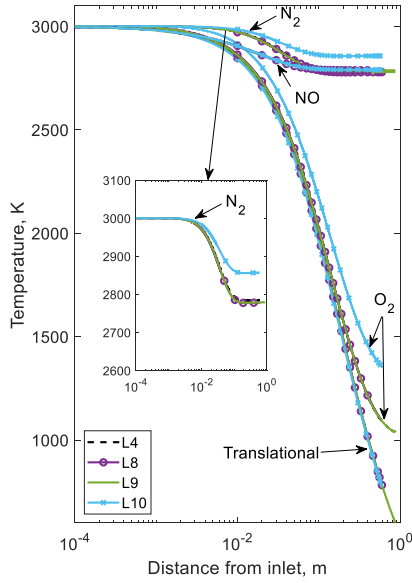
Fig. 3. Influence of multi-quantum transitions on the temperatures. The species vibrational temperatures shown are the average vibrational temperatures.
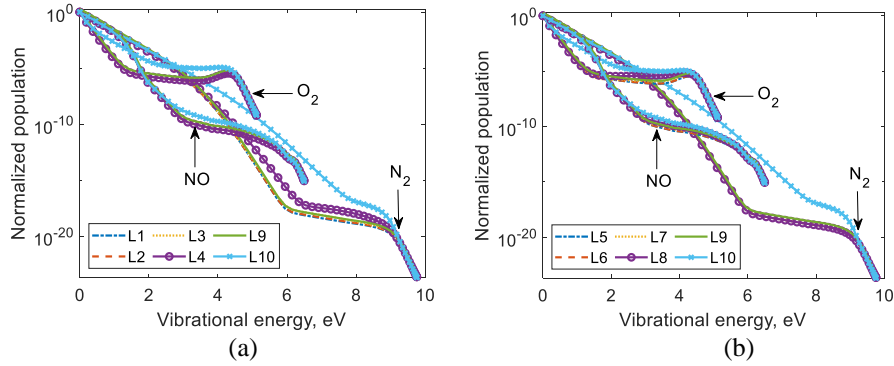

Fig. 4. Influence of multi-quantum transitions on the population distributions for the test cases (a) L1 to L4 and (b) L5 to L8 which represent the influence of N_2 and O_2 multi-quantum transitions respectively. These plots are extracted at 0.6 m from inlet which has A/A_{inlet} = 27.

All the tested quantum jump restrictions, including the single-quantum case (L10), produced negligible (less than 3 %) influences to the nozzle pressure, velocity, translational temperature and density profiles. This can be expected given the findings of Ref. [21, 23] for recombining nitrogen flows. The translational temperature profile is shown in Fig. 3 for the cases L4, L8, L9 and L10. The species mass fraction profiles are also uninfluenced by multi-quantum restrictions as they are basically frozen. More noticeable influences by multi-quantum restrictions can only be observed in the vibrational temperature profiles. Fig. 3 shows the average vibrational temperature obtained by solving the following equation for $T_{V,AB}$,

$$\sum_{v=0}^{v_{max}(AB)} \frac{\rho_{AB_v}}{\rho_{AB}} E_{AB_v} = \frac{\sum_{v=0}^{v_{max}(AB)} E_{AB_v} \exp\left(-\frac{E_{AB_v}}{k_B T_{v,AB}}\right)}{\sum_{v=0}^{v_{max}(AB)} \exp\left(-\frac{E_{AB_v}}{k_B T_{v,AB}}\right)} \tag{8}$$

where the energy of the nonequilibrium vibrational distribution equal the energy of a Boltzmann equilibrium vibrational distribution at the vibrational temperature $T_{V,AB}$. Even in this case, only the single-quantum transition case (L10) produced non-negligible changes in the O_2 and N_2 vibrational temperature profiles.

One has to look at the vibrational population distributions, shown in Fig. 4, in order to see any influences from the other restriction cases. But firstly, notice how the vibrational levels attain a population distribution in the shape of ｣ where a near "plateau" region forms around the intermediate levels. Caused by anharmonicity and coupling between the StS thermal and chemical kinetic processes [4, 70], this trend is commonly observed in nonequilibrium expanding flows as shown numerically [4, 21, 23, 44, 45, 47, 70-72], and experimentally [73, 74]. Sometimes, a small peak is formed on the right (higher level) side of the plateau region due to population inversion, as seen in O_2 in the current work and in Ref. [4, 21, 23, 44, 45, 47].

Now, from Fig. 4, the vibrational populations around the intermediate levels (around the aforementioned "plateau" region) are most influenced by the multi-quantum jump restrictions of Table 4. Some influences on the O_2 and N_2 vibrational populations can even be observed when their respective quantum jumps are restricted to 5 (case L4 and L8). The formation of different population distributions by the different cases is evident when examining the quantity $\frac{dc_i/dx}{c_i}$ where the mass fraction gradient of each pseudo-species, $\frac{dc_i}{dx}$, is normalized with its own mass fraction, c_i. The quantity $\frac{dc_i/dx}{c_i}$ is plotted in Fig. 5. Data at two locations are shown - 0.01 m and 0.1 m from the inlet. From this figure, it is obvious that the StS kinetics in the L4, L8 and L10 cases differ quantitively from those in the L9 (full multi-quantum set) case while exhibiting similar qualitative trends. Nevertheless, for the L4 and L8 cases, the resulting differences in the population distribution shown in Fig. 4 are not reflected in the vibrational temperature profiles because the differences, although visible in the log plots of Fig. 4, are too small to significantly influence the species vibrational energies and (consequently) the species vibrational temperatures.
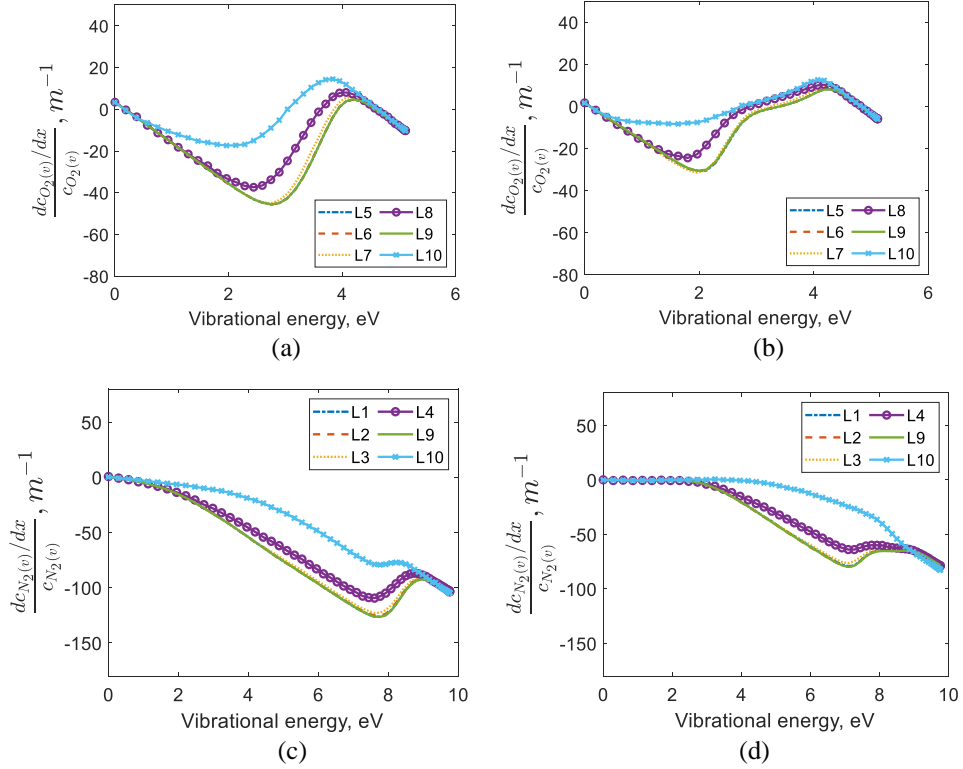
Fig. 5. The normalized mass fraction gradient, $\frac{dc_i/dx}{c_i}$, for (a) $O_2(v)$ at 0.01 m from the inlet, (b) $O_2(v)$ at 0.1 m from the inlet, (c) $N_2(v)$ at 0.01 m from the inlet, and (d) $N_2(v)$ at 0.1 m from the inlet.

Also, notice how Fig. 5 (d) shows that the N_2 lower vibrational levels (vibrational energy less than 3 eV) are essentially frozen at the distance of 0.1 m from the inlet. As a result, the N_2 vibrational temperature shown in Fig. 3 is frozen at this location, despite the higher levels still being reactive. This demonstrates that the vibrational energy and vibrational temperature are governed by the distribution of the lower energy levels as these levels generally have a much larger population. This can also be concluded when looking at the O_2 results in Fig. 5 where, despite the higher levels being less reactive compared to those of N_2, the lower levels remain reactive throughout the expansion leading to an O_2 vibrational temperature which is almost in equilibrium with the translational temperature, as shown in Fig. 3.
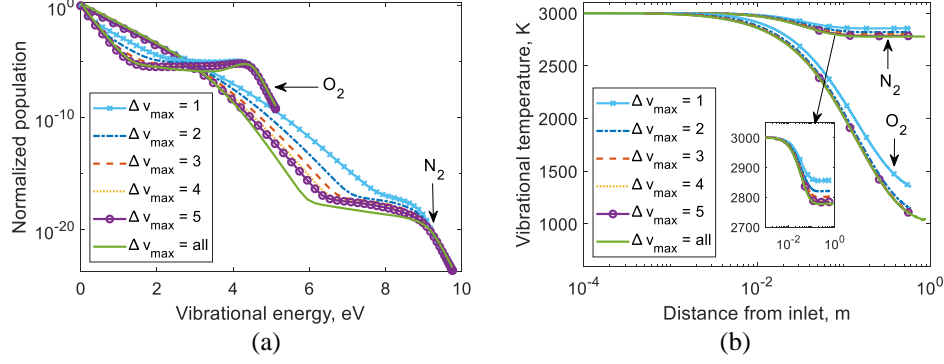
Fig. 6. Influence of multi-quantum transitions on the (a) population distributions and (b) vibrational temperatures for $\Delta v_{max,O2} = \Delta v_{max,N2} = \Delta v_{max} \in \{1,2,3,4,5,all\}$.

Overall, the results above show that limiting the multi-quantum jumps to 5 in both N_2 and O_2 can produce an accurate simulation of the nonequilibrium nozzle flow for most applications. Further simulations are conducted for $\Delta v_{max,O2} = \Delta v_{max,N2} = \Delta v_{max} \leqslant 5$ and the results are shown in Fig. 6. Looking at Fig. 6 (a), a big improvement in the population distribution is observed when the value of Δv_{max} is increased from 1 to 2. The incremental improvement gradually diminishes with higher values of Δv_{max}, showing an asymptotic behavior. Looking at Fig. 6 (b), one sees that limiting the multi-quantum jumps to 3 in both N_2 and O_2 ($\Delta v_{max,O2} = \Delta v_{max,N2} = \Delta v_{max} = 3$) yields vibrational temperatures which are basically indistinguishable from those of the full multi-quantum case ($\Delta v_{max} = all$).

Table 5.   Energy based multi-quantum transition cases

Case	$\Delta\epsilon_{max,O2}$, eV	$\Delta\epsilon_{max,N2}$, eV	No. of VVT transitions
E1	All	0.62	6×10^6
E2	0.62	All	1.6×10^7

In addition to the discussed quantum level-based approach to restricting the multi-quantum jumps, another approach involves restricting the quantum jumps based on the absolute energy difference between the vibrational levels involved in the VVT reaction. In other words, considering the VVT reaction $AB(i_1) + CD(i_2) \rightarrow AB(f_1) + CD(f_2)$, the absolute difference in vibrational level energy between $AB(i_1)$ and $AB(f_1)$, and between $CD(i_2)$ and $CD(f_2)$ cannot exceed some set values, $\Delta\epsilon_{max}$, in this approach. To compare this approach with the L4 and L8 test cases of the level-based approach, two test cases are created, denoted E1 and E2 respectively, as shown in Table 5. The value of $\Delta\epsilon_{max}$ is selected such that the total number of resulting VVT transitions matches with that of the corresponding level-based case (E1 with L4 and E2 with L8). As shown in Table 5, this involves restricting the possible quantum jumps

13

to less than or equal to 0.62 eV. By doing this, E1 and L4 have the same number of VVT transitions while E2 and L8 have the same number of VVT transitions.

The species vibrational energies and population distributions are assessed due to their sensitivity to the multi-quantum restrictions. The results in Fig. 7 show that, generally, the level-based criteria provides a better prediction than the energy-based criteria, given the same total number of VVT transitions. The application of the energy-based criteria on N_2 seems particularly bad, as shown in Fig. 7, where the E1 results are much worse than the L4 results despite having the same number of VVT transitions (6×10^6). In fact, the E1 results are close to the L10 results despite considering much more VVT transitions (L10 only has 6.7×10^4 transitions). The same finding has been made for pure N_2 and air in excitation heat bath and normal shock conditions respectively [49, 53].
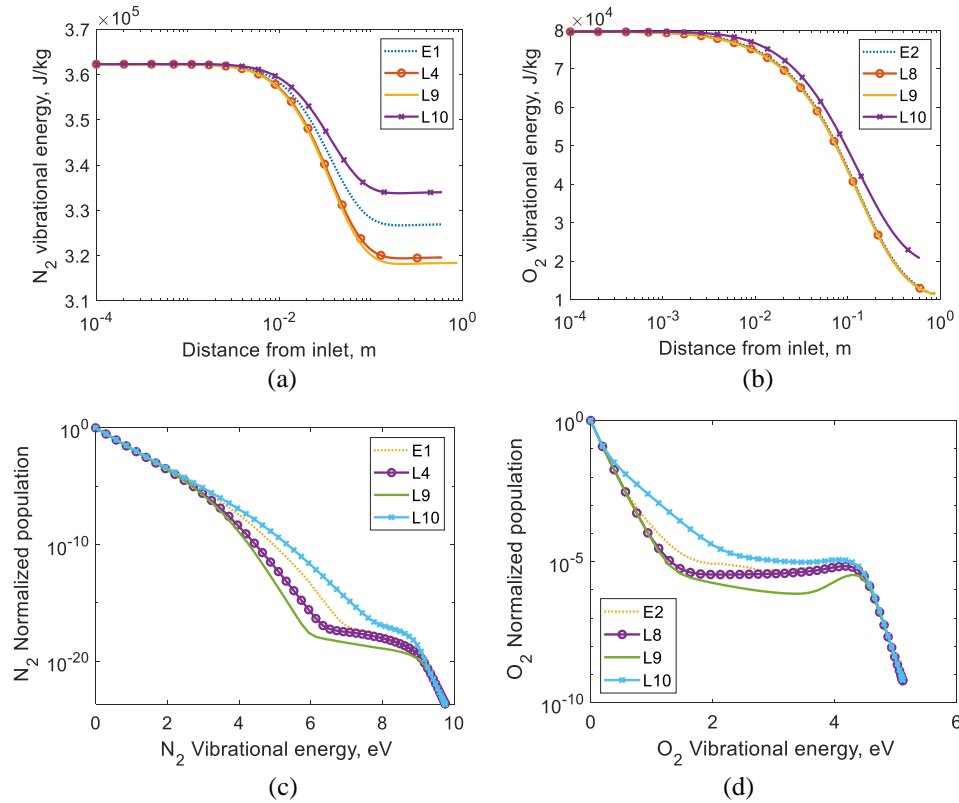

Fig. 7. Influence of multi-quantum transitions for the energy-based test cases. The species vibrational energies shown in (a) and (b) is per kg of gas mixture. The species population plots shown in (c) and (d) are extracted at 0.6 m from inlet which has A/A_inlet = 27.

Regarding the energy-based criteria, due to anharmonicity, there is a bias where more reactions (out of the total number of VVT reactions) involve the higher vibrational levels and less reactions involve the lower vibrational levels. Since the population of the higher levels is much lower than the population of the lower levels, it may be inappropriate to have more reactions involving the higher levels because the absolute rates of these reactions are very low. The

level-based criteria, thus, works better because it distributes the number of reactions evenly among all vibrational levels. An even better criteria would probably be one where more reactions (out of the total number of VVT reactions) involve the lower levels and less involve the higher energy levels, as discussed by Ref. [53, 75], which is the opposite of what we get when using the energy-based criteria.

B. Reducing VVT transitions to VT transitions

To reduce the number of transitions involved, as an alternative to restricting the quantum jumps of the VVT reactions, one may assume that the VVT processes occur as two independent VT processes such that the corresponding probability is given by [54, 55],

$$P(i_1, i_2 \rightarrow f_1, f_2) \approx P(i_1 \rightarrow f_1)P(i_2 \rightarrow f_2) \tag{9}$$

Summing over all of the possible vibrational states of the collision partner molecule,

$$P(i_1, all \rightarrow f_1, all) \approx P(i_1 \rightarrow f_1) \tag{10}$$

the VVT transitions reduce to VT transitions equivalent to that of molecule-atom collisions [48, 50-52]. The validity of this reduced order modelling is assessed in this section for a nozzle flow with the condition given in Table 3.
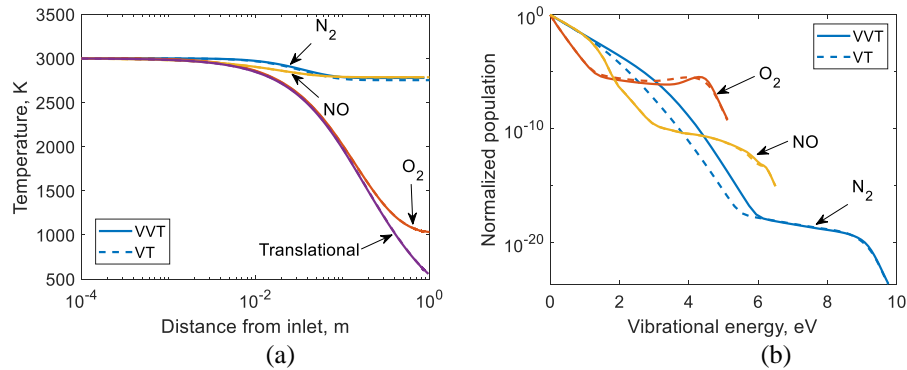

Fig. 8. Influence of VVT transitions on the (a) temperatures and (b) population distributions for the test case. Population plot extracted at 0.6 m from inlet which has A/A$_{inlet}$ = 27.

The results show that the reduction of VVT transitions to VT transitions is a good approximation in the current test case. Negligible differences in results are observed in the nozzle pressure, velocity, translational temperature and density profiles. The translational temperature profile can be seen in Fig. 8 (a). The species mass fraction profiles are also the same in both cases – frozen. One has to look at the vibrational population distribution in order to find any noticeable differences between the VVT and VT simulations. As shown in Fig. 8 (b), some differences are observed in the vibrational population of N_2 around the intermediate vibrational levels. This difference, however, is not enough to significantly influence the N_2 vibrational temperature as shown in Fig. 8 (a).

15

The possibility of reducing VVT transitions to VT transitions generally depends on the flow condition [21, 23]. Previous studies for normal shocks have shown equation 9 to be a poor approximation as the O_2 vibrational excitation rate was significantly increased when VVT transitions were reduced to VT transitions [48, 53]. However, the current nozzle flow is immune to this problem because O_2 maintains close to equilibrium with the translational mode. The previous studies also showed a slight increase in the N_2 vibrational excitation rate when VVT transitions were reduced to VT transitions [53]. However, the current nozzle flow is immune to this problem as well because the N_2 vibrational mode is almost frozen. As a result, the reduction of VVT transitions to VT transitions works well for the current condition. This finding is consistent with that reported by Ref. [70] for a converging-diverging nozzle with conditions representative of those in reflected shock tunnels, and that reported by Ref. [76] for a converging-diverging nozzle with a condition representative of those in arc-jets.

IV. Modelling of a real expansion tunnel condition

The StS model is now applied to a real X2 expansion tunnel condition designed and operated in Ref. [12], named "Air 1". The representative nozzle inlet condition, provided by Ref. [12], is shown in Table 6. The nozzle geometry and CFD estimated boundary layer edge is shown in Fig. 9. In the results presented later in this section, simulations are conducted using both of these contours. Exact coordinates are available for the nozzle contour while the boundary layer edge is extracted visually from the presented CFD density contour in Ref. [12] - higher precision on the extraction of the boundary layer edge is not desired anyway because the convergence of the CFD result is doubtful, as discussed by the author himself [12].

Table 6.   Nozzle inlet condition from Ref. [12].

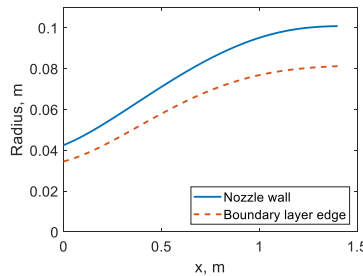| Inlet velocity, km/s	Inlet static pressure, kPa,	Inlet static temperature, K
8.0	20	3500

Fig. 9. Nozzle wall contour and boundary layer edge location.

The StS nozzle flow results are shown in Fig. 10 along with the results from the two-temperature (2T), thermochemical equilibrium (EQ), and calorically perfect gas (PG) simulations. In the 2T model, the Boltzmann distribution is assumed to exist within the vibrational modes. The vibrational modes are assumed to be tightly coupled among the molecules where they are described by a single vibrational temperature, T_v, while the translational and rotational modes are assumed to be tightly coupled where they are described by a single temperature, T. The vibrational-dissociation coupling model used is Park's [62] formulation. The species mass production term, $\dot{w}_1$, is calculated according to the modified Arrhenius equation which, for the dissociation/recombination reactions, is controlled by an effective temperature, T_c, given as $T_c = T^\phi T_v^{1-\phi}$ where $\phi = 0.5 - 0.7$. According to Ref. [77], ϕ is usually taken as 0.7, thus, the same is done in the current work. The vibrational energy conservation equation is expressed as [77-80],

$$de_v - \frac{dx}{\rho u}\left(\sum_{i=N_2,O_2,NO}\rho_i\frac{e_{v,i}^{eq} - e_{v,i}}{\tau_v} + e_{v,i}\dot{w}_1\right) = 0 \qquad (11)$$

where e_v and $e_{v,i}$ are the specific vibrational energies of the mixture and species i, respectively; and τ_v is the vibrational relaxation time calculated according to Park [62]. The above equation implies that molecules are created or destroyed at the average vibrational energy. The specific vibrational energies are computed assuming simple harmonic oscillators.

Firstly, from Fig. 10, the differences in the results obtained from using the nozzle wall contour (no BL) and boundary layer edge contour (BL) are negligible. This suggests that the current nonequilibrium flow is not particularly sensitive to the precise contour of the inviscid flow. The same finding was made by [5] who conducted the same analysis for a converging-diverging nozzle of a hypersonic blowdown facility.

From Fig. 10 (a), the translational temperature from the nonequilibrium simulations lies between the equilibrium and frozen bounds as expected. The higher translational temperature predicted by the two-temperature model indicates a faster relaxation compared to that of the StS model, which is consistent with normal shock and heat bath results [53, 81, 82]. This can also be seen in Fig. 10 (b) for the mole fraction profiles where slightly more recombination is seen in the 2T result which causes the higher translational temperature. Looking at the vibrational temperatures in Fig. 10 (c) and comparing with Fig. 10 (a), the 2T model predicts a thermal equilibrium condition while the StS model predicts thermal equilibrium (between translational and vibrational modes) for O_2 only. For N_2 and NO, the StS model predicts their vibrational temperature at the nozzle exit to be approximately 200 K and 500 K higher than the translational

temperature, respectively. Furthermore, as plotted in Fig. 10 (d), the StS model predicts a non-Boltzmann vibrational population distribution with over-population of the upper levels for all three molecules at the nozzle exit.
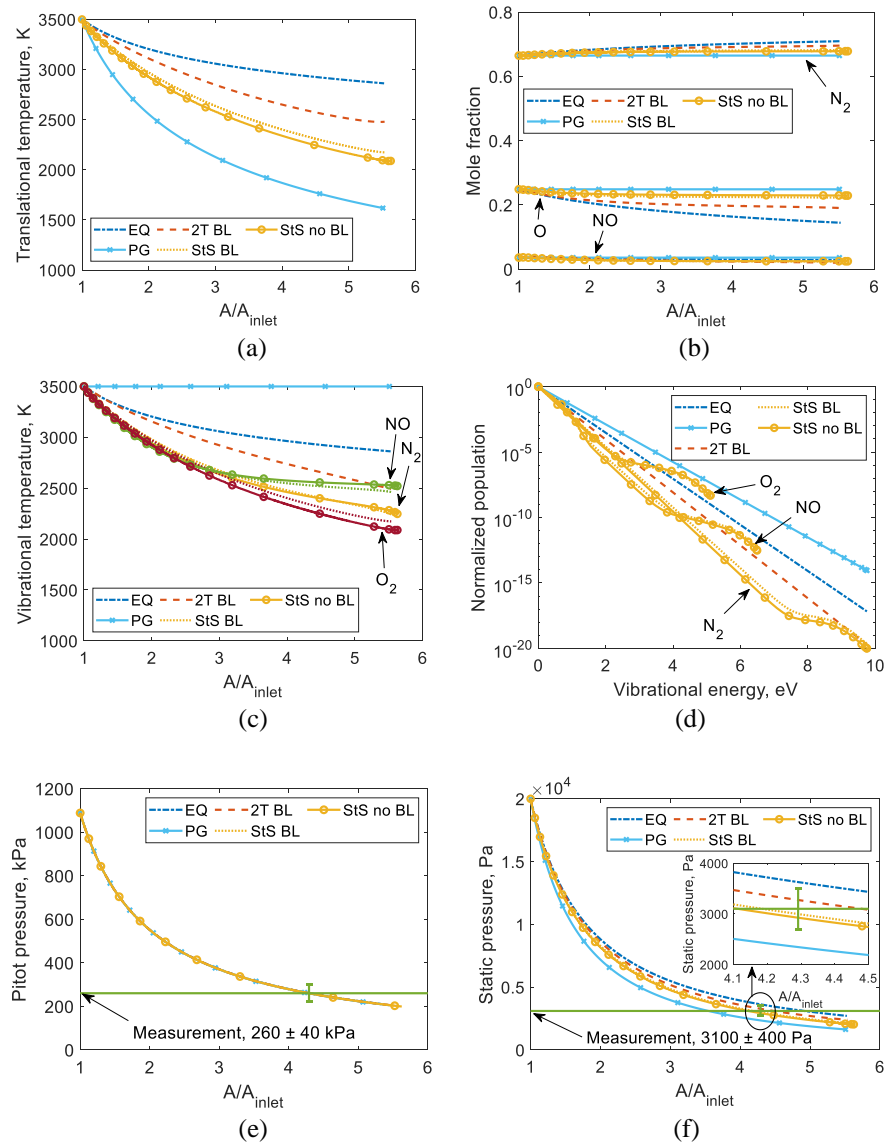

Fig. 10. Comparison of different thermochemical models on the nozzle flow (a) translational temperature, (b) mole fractions, (c) vibrational temperature, (d) vibrational population distributions, (e) pitot pressure, and (f) static pressure.

Ref. [12] provided a nozzle exit pitot pressure measurement: 260 ± 40 kPa. As shown in Fig. 10 (e), the pitot pressure is insensitive to the thermochemistry but is very sensitive to the nozzle area ratio; this is a well-known result [19, 83]. Consequently, comparing with the 200 kPa nozzle exit pitot pressure computed in the current work, the higher measured pitot pressure is indicative that the effective nozzle area ratio at the exit is slightly smaller than the ones given by the contours in Fig. 9. From Fig. 10 (e), the effective nozzle area ratio at the exit should be 4.3. Ref.

[12] also provided a nozzle exit static pressure measurement of 3.1 ± 0.4 kPa which agrees well with the nonequilibrium results computed in this work at the location of the effective nozzle exit area ratio, as shown in Fig. 10 (f). However, due to the small differences in the nonequilibrium results and the relatively large uncertainty in the measurement, no further information can be obtained from the static pressure. It is also acknowledged that the basis of this discussion is that the inflow condition in Table 6, provided by Ref. [12], is accurate.

Based on the results presented in this section, it may be possible to suggest that one can produce an accurate estimate of the nozzle exit condition with a quasi-one-dimensional analysis using the effective nozzle area ratio without knowing the precise contour of the inviscid flow (a rough estimate of the contour is probably adequate). Nevertheless, an accurate thermochemical nonequilibrium model is still required. In addition to the static pressure, the temperatures (vibrational and translational) are also sensitive to thermochemical nonequilibrium, as shown in Fig. 10 (a) and (c). Unfortunately, no temperature measurements are available to allow evaluation of the different thermochemical models. Thus, a study is conducted in the next section to examine the potential implications of the different nozzle exit conditions produced by the different thermochemical models.

V. Effect of freestream thermochemical excitation on a normal shock flow

As shown in Fig. 10, for the same nozzle geometry and area ratio, different thermochemical models produce different nozzle exit conditions. It is of interest to expansion tunnel operators to understand the implications of the different nozzle exit conditions, and how these implications can potentially affect experiments conducted in this type of facility. In this section, we will investigate how the different nozzle exit conditions can influence the flow behind a normal shock.

Experimental studies of normal shock flows are traditionally done in a shock tube with a moving shock; the freestream condition is in thermochemical equilibrium at room temperature and is accurately characterized. Alternatively, researchers at The University of Queensland have used a conical shock generator test model in an expansion tunnel, producing a Mach disk [84]. This approach is advantageous in that the standing shock allows for a longer imaging time which would not be possible if the shock is moving due to smearing. While this can also be achieved using a blunt body to generate a bow shock, the space behind the Mach disk allows the entire equilibration process to be observed which cannot be achieved using the bow shock's stagnation streamline unless very large test models and/or freestream densities can be realized.
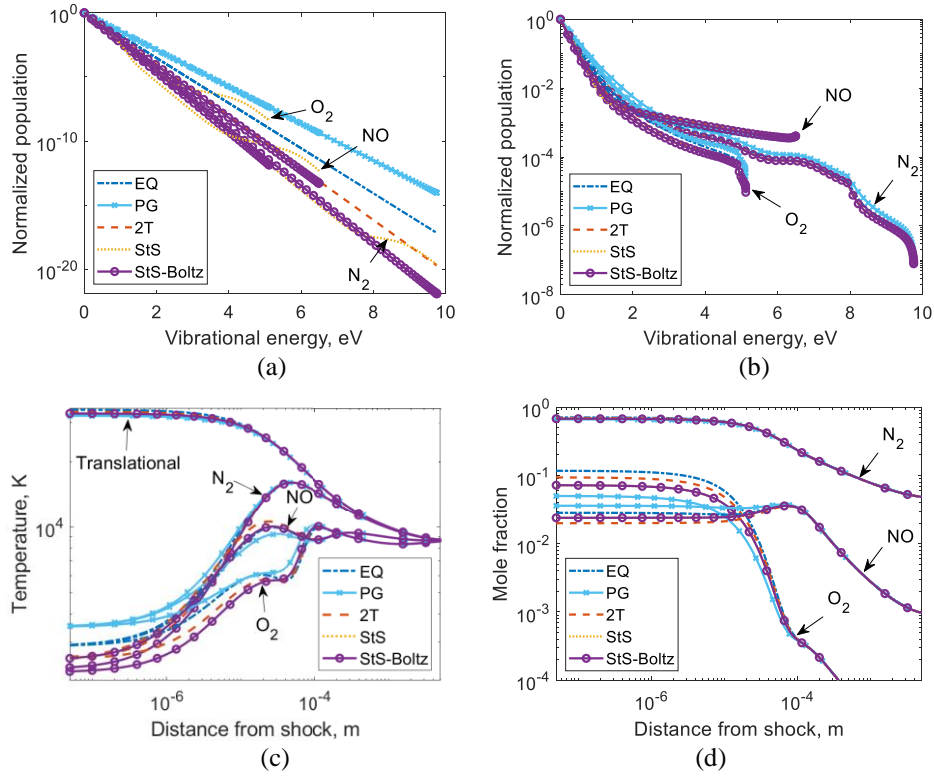
19

Fig. 11. Effect of different freestream thermochemical excitation on a normal shock flow. Plot (a) and (b) shows the vibrational population distribution immediately behind the shock and at 10⁻⁶ m behind the shock respectively. Plots (c) and (d) shows the post-shock temperatures and mole fractions.

So, in anticipation of future Mach disk experiments in expansion tunnels, StS normal shock simulations are conducted using the same numerical model described in section II ('A' in equation 1 is removed as a constant), including full VVT transitions (required for normal shocks [48, 53]), with the initial post-shock condition calculated from the Rankine-Hugoniot relations. Several freestream conditions are tested which are extracted correspondingly from the 'EQ', 'PG', '2T BL', and 'StS BL' results at the effective nozzle area ratio from the previous section. An additional freestream condition – 'StS-Boltz' – is introduced, which is a variation of the 'StS BL' result, where the vibrational population distribution is transformed into a Boltzmann distribution at the same average vibrational temperature. Again, five species (N_2, O_2 N, O and NO) are considered and only the ground electronic state is considered for all species. This should be valid since Ref. [60, 85, 86] showed that, for similar conditions ($h_0 \approx 35$ MJ/kg), ionization and electronic excitation do not play a major role in the thermochemistry of the flow behind a normal shock.

Fig. 11 (a) shows the vibrational population distributions immediately behind the shock. In the 'EQ', 'PG' and '2T' cases, the different molecular species have the same initial vibrational temperature, thus, their O_2, N_2 and NO

distributions overlap in the plot. Looking at Fig. 11 (b), after only 10^{-6} m which is prior to any significant vibrational excitation and dissociation as shown in Fig. 11 (c) and (d) respectively, the higher levels from the different cases have already achieved approximately the same distribution while the lower levels remain approximately frozen as reflected in the vibrational temperature. Beyond 10^{-6} m, vibrational excitation and dissociation begins and the results from the five different freestreams converge by 10^{-4} m. So, the general trend is that the largest discrepancies among the results from the different freestream conditions are observed immediately behind the shock. The discrepancies vanish as the flow equilibrates, eventually reaching the same equilibrium condition because all five freestream conditions have exactly the same total enthalpy. Also, no difference can be observed between the 'StS' and 'StS-Boltz' results, indicating that the non-Boltzmann distributions in the freestream has no influence on the post-shock flow.
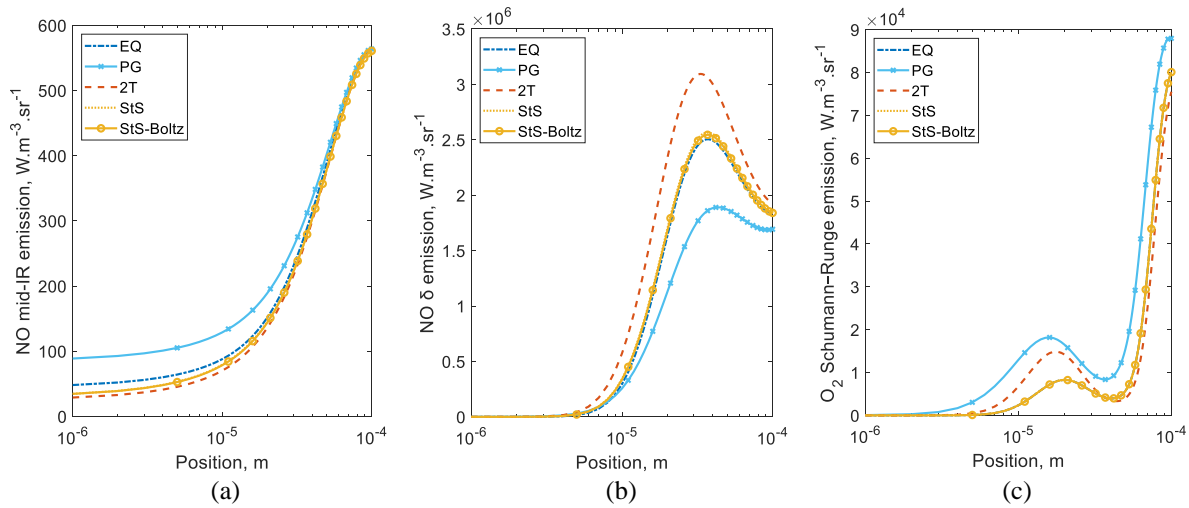

Fig. 12. Effect of different freestream thermochemical excitation on the post-shock (a) NO mid-IR, (b) NO δ, and (c) O₂ Schumann-Runge emissions.

From inspection of the results in Fig. 11 (c) and (d), one can observe that the most sensitive parameters to the freestream conditions are the vibrational temperature and mole fraction of NO and O_2. Both are important parameters for the radiation emission. Thus, to provide a rough engineering approximate to show how the post-shock radiation emission varies with the different freestream conditions, emissions were computed using SPARK (Simulation Platform for Aerodynamics, Radiation and Kinetics) [87]. The NO mid-infrared (mid-IR), NO δ band, and O_2 Schumann–Runge bands are simulated, with the spectrally integrated results shown in Fig. 12 (a), (b), and (c) respectively. The NO mid-IR emission originates from the NO vibrational mode which is modelled in the current analysis. However, the NO δ band and O_2 Schumann–Runge bands originate from the electronic modes which are not modelled. Thus, when computing the NO δ band and O_2 Schumann–Runge bands, the electronic level population is

assumed to have a Boltzmann distribution according to the vibrational temperature, which is a reasonable approximation made when wanting a rough engineering estimate [4, 60, 62, 86, 88].

Looking at the NO mid-IR emission in Fig. 12 (a), the 'PG' freestream initially gives an emission twice as high as the other results, but all results gradually converge by 10^{-4} m. The differences here are mainly driven by the differences in the NO mole fractions shown in Fig. 11 (d). For the NO δ band shown in Fig. 12 (b), the peak emission differs by as much as 40 % between the various freestreams, where this maximum difference is observed when comparing between the '2T' freestream and the 'PG' freestream cases. The differences here are mainly driven by the differences in the NO vibrational temperature shown in Fig. 11 (c). Even when comparing between the '2T' freestream and StS freestream cases, a difference of 20 % is observed in the emission despite the close similarity of these two freestream conditions as shown in Fig. 10. Looking at the O_2 Schumann–Runge emission in Fig. 12 (c) and examining the small peak at around 2 x 10^{-5} m which is caused by the rapid O_2 decomposition pausing the excitation process until most of O_2 is dissociated as shown in Fig. 11 (c) and (d), the emission at this peak can differ by more than 50 % among the various freestream cases. The differences here are mainly driven by the differences in the O_2 vibrational temperature as shown in Fig. 11 (c). Even when comparing between the '2T' freestream and StS freestream cases, a difference of 40 % is observed in the emission. Lastly, all the results in Fig. 12 show no difference between the 'StS' and 'StS-Boltz' freestream cases, further indicating that the non-Boltzmann distributions in the freestream has no influence on the post-shock flow.

Overall, the results in Fig. 12 demonstrate the sensitivity of the post-shock radiation emission to the freestream condition and reveal the subsequent difficulty encountered when studying the post-shock emission in an expansion tunnel due to the uncertainty of the test conditions. Consequently, as discussed in section IV, temperature (translational and/or vibrational) measurements at the nozzle exit are desired in the future to validate thermochemical nonequilibrium models for predicting the correct nozzle exit conditions in order to reduce the uncertainties of the test conditions and allow for better interpretation of experimental results.

Studies similar to the work of the current section have been conducted in the past by other authors, looking at the differences between the thermochemically excited test condition of the reflected shock tunnel (which suffer more from thermochemical excitation due to stagnation of the test gas [3]) and the equivalent flight condition. This is done by Ref. [19, 89-92] for the bow shock, Ref. [4] for the normal shock, and Ref. [18] for shock-boundary layer interactions. Ref. [91, 92] showed that freestream thermochemical excitation leads to a reduced density jump across a shock

resulting in a larger shock stand-off distance compared to flight, while Ref. [90] showed that the elevated translational temperature produced in shock tunnels results in a failure to reproduce the aerodynamic forces in flight. Additionally, Ref. [18] showed that freestream vibrational excitation quantitatively influences shock-boundary layer interactions. Furthermore, Ref. [4] concluded that the thermochemical excitation frozen in the reflected shock tunnel freestream "causes the relaxation behind a normal shock wave to be generally different from that in free flight".

Which flight equivalent flow properties can be reproduced in hypersonic ground-test facilities is described by Ref. [90] as an "important" and "difficult" question to answer. As a contribution to addressing this question, a corollary of the results in Fig. 12 is that the expansion tunnel, in general, probably cannot be used to quantitatively reproduce entirely the radiation emission of an equivalent flight condition. This is due to the influence of the freestream thermochemical excitation, which generally cannot be matched with flight. Nevertheless, this facility remains vital for fundamental studies and validation of general models for radiation.

VI. Comparison between 2T and StS models

Despite the recent advances in high performance computing, two- and three-dimensional nozzle simulations relevant to hypersonic ground-test facilities generally still employ the low fidelity 2T (or even 1T) model for engineering and design purposes [41, 83, 93]. Therefore, it is of interest to provide a comprehensive evaluation of the discrepancy between the 2T and StS models, and assess the possibility of modifying the 2T model to give results closer to those of the StS model. These are addressed in the current section for the expansion tunnel nozzle.

Table 7.   Test conditions for comparing 2T and StS models.

Case	Inlet static pressure, kPa,	Inlet static temperature, K	Inlet species mass fractions
1	10	2500	N_2:0.75, O_2:0.22
2	100	2500	N_2:0.75, O_2:0.23
3	10	4000	N_2:0.74, O_2:0.01
4	100	4000	N_2:0.73, O_2:0.04

From inspection of the species continuity equation in equation 1 and the rate equations of equations 2 – 6, one can see that the thermochemical kinetics, dc_i/dx, is related to u and ρ. The value of dc_i/dx is inversely proportional to u. The value of dc_i/dx is proportional to ρ for the VT and VVT reactions, and the value of dc_i/dx is proportional to ρ^2 for the recombination reactions. Since p is proportional to ρ according to the ideal gas law, the aforementioned trends for ρ can also be said for p. In the expansion tunnel, the nozzle inlet pressure typically ranges from around 10 kPa to 100 kPa [94-97], while the nozzle inlet velocity typically ranges from around 4 km/s to 11 km/s [95, 98, 99]. Based on these conditions and the discussion on the dependencies of dc_i/dx, we can see that it is the range of the inlet pressure

(an order of magnitude, which is much higher than the factor of 2-3 for the range of the inlet velocity) which would determine the variety of different thermochemical behaviors (equilibrium, frozen, nonequilibrium) that are possible in the expansion tunnel nozzle. Therefore, evaluations of the discrepancy between the 2T and StS models are carried out for the entire range of the inlet pressure. The nozzle inlet temperature typically ranges from around 1000 K to up to 4000 K [95, 100]. However, the StS reaction rates determined from the FHO theory, which are used in this work, are less accurate at low temperatures ($\lesssim 1000$ K) due to pronounced quantum effects (such as anti-Arrhenius behavior) which are not accounted for [53, 101]. As a result, the conditions tested for the current study are listed in Table 7 where the inlet temperature is restricted to a minimum of 2500 K. The inlet velocity is a constant at 7.5 km/s (the midrange) and the nozzle geometry is the wall contour (no boundary layer) of the X2 expansion tunnel nozzle shown in Fig. 9.
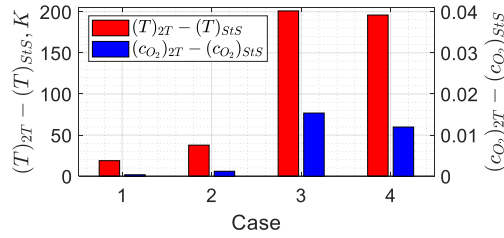

Fig. 13. The differences in the computed nozzle exit translational temperature, T, and O_2 mass fraction, c_{O_2}, between the 2T and StS simulations.

From the results, negligible differences of less than 1 % are observed in the nozzle exit velocities and densities, between the 2T and StS simulations. The nozzle exit translational temperature, however, can differ by almost 10 % between the two models. Since the translational temperature is related to the static pressure via $p = \rho R T$, and the nozzle exit ρ and R hardly vary between the 2T and StS results, the (up to) 10 % differences in the exit translational temperature leads to the same for the exit static pressure.

From Fig. 13, one can see that the 2T model, when compared with the StS model, generally predicts a higher nozzle exit translational temperature. This, when seen in a nozzle flow, is indicative of a faster thermochemical relaxation in the 2T model. The faster relaxation in the 2T model has already been demonstrated in section IV and in Ref. [53, 81, 82]. The faster relaxation causes more recombination which leads to a higher nozzle exit O_2 mass fraction in the 2T result as shown in Fig. 13. For cases 1 and 2, the differences in the nozzle exit translational temperature between the 2T and StS results is small (< 50 K) because there is minimal dissociation at the nozzle inlet as shown in Table 7 (inlet temperature is 2500 K) and, therefore, the differences in the relaxation rates between the two models

are not manifested obviously in the translational temperature. On the other hand, for cases 3 and 4, there is more

dissociation at the nozzle inlet as shown in Table 7 (inlet temperature is 4000 K where O_2 is significantly dissociated

although nitrogen remain almost undissociated) and, therefore, a larger difference of around 200 K is observed for the

nozzle exit translational temperature between the 2T and StS results. Likewise, a small (< 0.002) difference in the

nozzle exit O_2 mass fraction is seen between the 2T and StS results for cases 1 and 2 because O_2 is hardly dissociated

in the first place, while a larger difference of around 0.013 is seen for cases 3 and 4 because O_2 is significantly

dissociated at the inlet.

Also, from Fig. 13, one can see that the degree of discrepancy (or agreement) between the 2T and StS models is

not particularly sensitive to the inlet static pressure. Comparing between cases 1 and 2, and between cases 3 and 4, the

differences in the discrepancies between the 2T and StS models for the nozzle exit translational temperature and O_2

mass fraction are less than 20 K and 0.004, respectively. As a corollary, one may say that the degree of discrepancy

between the 2T and StS models is also not particularly sensitive to the inlet velocity, which has a similar influence on

the thermochemical kinetics and a much smaller range for variations compared to the inlet static pressure, as discussed
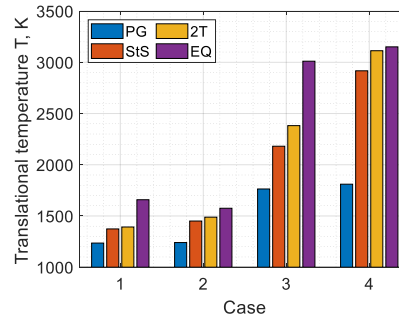
earlier.

Fig. 14. The nozzle exit translational temperature, T.

As discussed in section IV and in Ref. [102], the translational temperature in a nozzle flow is bounded by the

thermochemically frozen (lower bound) and thermochemical equilibrium (upper bound) solutions. Looking at Fig. 14

and comparing between cases 1 and 2, and between cases 3 and 4, one can see that increasing the nozzle inlet pressure

urges the thermochemical kinetics in the nozzle flow towards the equilibrium bound, as expected. For the special case

of case 4, where the inlet temperature and pressure are both high, the nozzle flow approaches near the equilibrium

bound. Although the nozzle inlet pressure here already represents (approximately) the upper bound for a realistic

expansion tunnel, if even greater inlet pressures are theoretically used, then the nozzle flow would be well in

thermochemical equilibrium. In such a case, whichever finite rate model (2T or StS) is used in the simulation would be unimportant as it would have no influence on the result. Likewise, if a nozzle inlet pressure significantly lower than 10 kPa is theoretically used, then the nozzle flow would be thermochemically frozen. Again, in such a case, whichever finite rate model is used would have no influence on the result. Nevertheless, as shown in Fig. 14, most of the operating conditions in a realistic expansion tunnel would be in nonequilibrium where the choice of the finite rate model would make a difference to the nozzle flow simulation. Appropriate tuning of the rates used in the 2T model could allow for agreement with the StS model for the translational temperature and species mass fractions. However, further considerations are required to deal with the species vibrational temperatures.
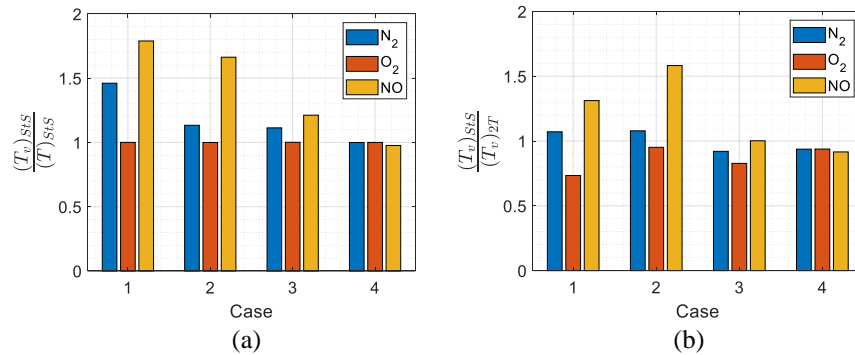

Fig. 15. The normalized nozzle exit species vibrational temperatures from the StS simulations, where (a) is normalized with the corresponding nozzle exit translational temperature, T, and (b) is normalized with the corresponding nozzle exit vibrational temperature from the 2T simulations.

In the 2T model, the vibrational modes are assumed to be tightly coupled among the molecules where they are described by a single vibrational temperature. Previous studies on heat bath and post-shock conditions have shown this to be a poor assumption [50, 53, 60, 81, 103]. The validity of this assumption for expansion tunnel nozzle flows can be assessed by examining Fig. 15 (a). One can see that, in general, the molecular species all have a different vibrational temperature. This is particularly the case for the lower nozzle inlet temperature conditions (cases 1 and 2) where the vibrational temperatures among the species can differ by up to 80 %. The validity of the assumption does improve with increasing nozzle inlet temperature as this difference is reduced to less than 20 % in the higher nozzle inlet temperature conditions (cases 3 and 4). The validity of the assumption also improves with increasing nozzle inlet pressure, as seen when comparing between cases 1 and 2, and between cases 3 and 4, because the higher pressure promotes equilibration.

Fig. 15 (b) quantifies the discrepancy in the prediction of the nozzle exit vibrational excitation between the 2T and StS models. For the lower inlet temperature cases, the T_v from the 2T model can underpredict the StS vibrational

temperature of N_2 by up to 10 % and NO by up to 60 % while it can overpredict the StS vibrational temperature of O_2 by up to 30 %. For the higher inlet temperature cases, the T_v from the 2T model is generally equal to or greater than the StS species vibrational temperatures by no more than 20 %.

As shown in section V and in Ref. [4, 18], predicting the correct vibrational excitation at the nozzle exit is important for the correct interpretation of certain experiments. However, also shown in section V is that the non-Boltzmann distributions at the nozzle exit is rather unimportant. This means that suitable multi-temperature (Boltzmann) models with appropriately tuned thermochemical rates are potentially sufficient for predicting expansion tunnel nozzle exit conditions for the intent and purposes relevant to wind tunnel experimentations. As shown in Fig. 15 and discussed above, the 2T model with a single vibrational temperature is not suitable. Examining Fig. 15 (a), it may be concluded that a three-temperature model is generally required, where one temperature describes the translational, rotational and O_2 vibrational modes, one describes the N_2 vibrational mode, and one describes the NO vibrational mode. If one wants to consider NO as a minor species and, thus, as being less important (perhaps for aerodynamic studies for example), an alternative two-temperature model may be proposed where one temperature describes the translational, rotational and O_2 vibrational modes, and one describes the N_2 and NO vibrational modes (with tightly coupled assumed among the N_2 and NO molecules where they are described by a single vibrational temperature). For the special case where the inlet pressure and temperature are both high, as demonstrated by case 4 in Fig. 15 (a), a one-temperature model is sufficient.

VII. Conclusions

Thermochemical nonequilibrium in expansion tunnel nozzles is investigated numerically using a state-to-state description in one-dimension for representative air conditions. A parametric study is performed to examine the influence of multi-quantum VVT transitions, and the validity of simplifying VVT transitions to VT transitions. Overall, the results show that limiting the multi-quantum jumps of VVT transitions to 3 in both N_2 and O_2 can produce an accurate simulation of the nonequilibrium nozzle flow. The results also show that the reduction of VVT transitions to VT transitions works well for the considered nozzle simulation.

Then, state-specific modelling of an actual expansion tunnel nozzle condition is conducted. Agreement with the measured nozzle exit static pressure is observed within the measurement uncertainty. However, due to the relatively large uncertainty, this agreement is also observed when using the 2T model. Thus, it is of interest to quantify the influence of different thermochemical excitations in the freestream on the flow behind a normal shock at the expansion

tunnel test section. The most sensitive post-shock parameters to the freestream conditions are the vibrational temperature and mole fraction of NO and O_2, which results in differences of more than 50 % among the post-shock emissions calculated from the different freestream conditions. In particular, when comparing between the emissions computed from the '2T' and 'StS' freestreams, differences of up to 40 % are observed even though the freestream static pressure of these two conditions both agree, within the uncertainty, with the experimental measurement. This demonstrates the difficulty one would encounter when studying radiation emissions in an expansion tunnel. Nevertheless, no difference can be observed between any of the 'StS' and 'StS-Boltz' post-shock results, indicating the non-Boltzmann distributions in the freestream has no influence. This means that suitable multi-temperature (Boltzmann) models with appropriately tuned thermochemical rates are potentially sufficient for predicting expansion tunnel nozzle exit conditions for the intent and purposes relevant to wind tunnel experimentations.

Subsequently, a comprehensive evaluation of the discrepancy between the 2T and StS models is carried out, and the possibility of modifying the 2T model to give results closer to those of the StS model is assessed. Compared to the StS model, the 2T model generally predicts a faster thermochemical relaxation which in turn results in a higher static temperature and greater molecular mass fractions at the exit of nozzle flows. The degree of discrepancy (or agreement) between the 2T and StS models is not particularly sensitive to the inlet static pressure and velocity. Appropriate tuning of the rates used in the 2T model could allow for agreement with the StS model for the translational temperature and species mass fractions. However, further considerations are required to deal with the species vibrational temperatures. The StS results indicate that, in general, the molecular species all have a different vibrational temperature which means that the 2T model with a single vibrational temperature is not suitable. It may be concluded that a three-temperature model is generally required, where one temperature describes the translational, rotational and O_2 vibrational modes, one describes the N_2 vibrational mode, and one describes the NO vibrational mode.

Acknowledgements

References

1.   Trimpi, R. L., and Callis, L. B. "A Perfect-gas Analysis of the Expansion Tunnel: A Modification to the Expansion Tube." NASA TR R-223, NASA Langley Research Center, Langley Station, Hampton, VA, USA, 1965.

2.   Sharma, S. P., and Park, C. "Operating characteristics of a 60-and 10-cm electric arc-driven shock tube-part II: the driven section," *Journal of thermophysics and heat transfer* Vol. 4, No. 3, 1990, pp. 266-272. https://doi.org/10.2514/3.56243

3.   Gu, S., and Olivier, H. "Capabilities and limitations of existing hypersonic facilities," *Progress in Aerospace Sciences* Vol. 113, 2020, p. 100607.
https://doi.org/10.1016/j.paerosci.2020.100607

4.   Park, C. "Thermochemical relaxation in shock tunnels," *Journal of thermophysics and heat transfer* Vol. 20, No. 4, 2006, pp. 689-698.
https://doi.org/10.2514/1.22719

5.   Gimelshein, S. F., and Wysong, I. J. "Nonequilibrium effects in high enthalpy gas flows expanding through nozzles," *Physics of Fluids* Vol. 33, No. 10, 2021, p. 106104.
https://doi.org/10.1063/5.0068917

6.   James, C., Gildfind, D., Lewis, S., Morgan, R., and Zander, F. "Implementation of a state-to-state analytical framework for the calculation of expansion tube flow properties," *Shock Waves*, 2017, pp. 1-29.
https://doi.org/10.1007/s00193-017-0763-3

7.   Neely, A., and Morgan, R. "The superorbital expansion tube concept, experiment and analysis," *The Aeronautical Journal* Vol. 98, No. 973, 1994, pp. 97-105.
https://doi.org/10.1017/S0001924000050107

8.   Dufrene, A., Sharma, M., and Austin, J. "Design and characterization of a hypervelocity expansion tube facility," *Journal of Propulsion and Power* Vol. 23, No. 6, 2007, pp. 1185-1193.
https://doi.org/10.2514/1.30349

9.   Neely, A., Stalker, R., and Paull, A. "High enthalpy, hypervelocity flows of air and argon in an expansion tube," *The Aeronautical Journal* Vol. 95, No. 946, 1991, pp. 175-186.
https://doi.org/10.1017/S0001924000023885

10.   Miller, C. G. "Operational experience in the Langley expansion tube with various test gases," *AIAA Journal* Vol. 16, No. 3, 1978, pp. 195-196.
https://doi.org/10.2514/3.60877

11.   Gildfind, D., Jacobs, P., Morgan, R., Chan, W., and Gollan, R. "Scramjet test flow reconstruction for a large-scale expansion tube, Part 2: axisymmetric CFD analysis," *Shock Waves* Vol. 28, No. 4, 2018, pp. 899-918.
https://doi.org/10.1007/s00193-017-0786-9

12.   Scott, M. P. "Development and modelling of expansion tubes," *Centre for Hypersonics, Dept. of Mechanical and Mining Engineering*. PhD Thesis, Univ. of Queensland, Brisbane, Queensland, Australia, 2007.

13.   Wheatley, V., Chiu, H., Jacobs, P. A., Macrossan, M. N., Mee, D. J., and Morgan, R. G. "Rarefied, superorbital flows in an expansion tube," *International Journal of Numerical Methods for Heat & Fluid Flow* Vol. 14, No. 4, 2004, pp. 512-537.
https://doi.org/10.1108/09615530410532277

14.   Chinitz, W., Erdos, J. I., Rizkalla, O., Anderson, G., and Bushnell, D. M. "Facility opportunities and associated stream chemistry considerations for hypersonic air-breathing propulsion," *Journal of Propulsion and Power* Vol. 10, No. 1, 1994, pp. 6-17.
https://doi.org/10.2514/3.23705

15.   Park, C. *Nonequilibrium hypersonic aerothermodynamics*. New York: Wiley, 1989.

16.   Olivier, H., and Gu, S. "Operation, Capabilities and Limitations of Existing Hypersonic Facilities," *VKI Lecture Series: Flow characterization and modeling of hypersonic wind tunnels*. STO-EN AVT-325-01, von Karman Institute for Fluid Dynamics, Sint-Genesius-Rode, Belgium, 2018.

17.   Reynier, P. "Survey of high-enthalpy shock facilities in the perspective of radiation and chemical kinetics investigations," *Progress in Aerospace Sciences* Vol. 85, 2016, pp. 1-32.
https://doi.org/10.1016/j.paerosci.2016.04.002

18.   Nompelis, I., Candler, G. V., and Holden, M. S. "Effect of vibrational nonequilibrium on hypersonic double-cone experiments," *AIAA journal* Vol. 41, No. 11, 2003, pp. 2162-2169.

https://doi.org/10.2514/2.6834

19.   Hall, J. G., and Treanor, C. E. "Nonequilibrium effects in supersonic-nozzle flows." AGARDograph No. 124, 1967.

20.   Colonna, G. "Problems and perspectives of state-to-state kinetics for high enthalpy plasma flows," *AIP Conference Proceedings*. Vol. 1628, American Institute of Physics, 2014, pp. 1176-1185.
       http://dx.doi.org/10.1063/1.4902726.

21.   Colonna, G., Armenise, I., Bruno, D., and Capitelli, M. "Reduction of state-to-state kinetics to macroscopic models in hypersonic flows," *Journal of thermophysics and heat transfer* Vol. 20, No. 3, 2006, pp. 477-486.
       https://doi.org/10.2514/1.18377

22.   Colonna, G., Bonelli, F., and Pascazio, G. "Impact of fundamental molecular kinetics on macroscopic properties of high-enthalpy flows: The case of hypersonic atmospheric entry," *Physical Review Fluids* Vol. 4, No. 3, 2019, p. 033404.
       https://doi.org/10.1103/PhysRevFluids.4.033404

23.   Colonna, G., Pietanza, L. D., and Capitelli, M. "Recombination-assisted nitrogen dissociation rates under nonequilibrium conditions," *Journal of Thermophysics and Heat Transfer* Vol. 22, No. 3, 2008, pp. 399-406.
       https://doi.org/10.2514/1.33505

24.   Cutrone, L., Tuttafesta, M., Capitelli, M., Schettino, A., Pascazio, G., and Colonna, G. "3D nozzle flow simulations including state-to-state kinetics calculation," *AIP Conference Proceedings*. Vol. 1628, American Institute of Physics, 2014, pp. 1154-1161.
       https://doi.org/10.1063/1.4902723.

25.   Ninni, D., Bonelli, F., Colonna, G., and Pascazio, G. "Unsteady behavior and thermochemical non equilibrium effects in hypersonic double-wedge flows," *Acta Astronautica* Vol. 191, 2022, pp. 178-192.
       https://doi.org/10.1016/j.actaastro.2021.10.040

26.   Tuttafesta, M., Pascazio, G., and Colonna, G. "Multi-GPU unsteady 2D flow simulation coupled with a state-to-state chemical kinetics," *Computer Physics Communications* Vol. 207, 2016, pp. 243-257.
       https://doi.org/10.1016/j.cpc.2016.07.016

27.   Morgan, R., Neely, A., and Scott, M. "Hypervelocity Carbon Dioxide Flow Simulation," *Shock Waves@ Marseille II*. Vol. 2, Springer, Berlin, 1995, pp. 217-222.

28.   Hollis, B. R., Prabhu, D. K., Maclean, M., and Dufrene, A. "Blunt-Body Aerothermodynamic Database from High-Enthalpy Carbon-Dioxide Testing in an Expansion Tunnel," *Journal of Thermophysics and Heat Transfer* Vol. 31, No. 3, 2017.
       https://doi.org/10.2514/1.T5019

29.   Gu, S., Morgan, R. G., McIntyre, T. J., and Brandis, A. M. "An Experimental Study of CO2 Thermochemical Nonequilibrium," *AIAA Journal* Vol. Articles in Advance, 2021.
       https://doi.org/10.2514/1.J061037

30.   Wegener, M., Sutcliffe, M., Morgan, R., McIntyre, T., and Rubinsztein-Dunlop, H. "Diagnostics of a range of highly superorbital carbon dioxide flows," *39th Aerospace Sciences Meeting and Exhibit*. AIAA Paper 2001-0304, January 2001.
       https://doi.org/10.2514/6.2001-304.

31.   Jones, J. J. "Some performance characteristics of the LRC 3 3/4-inch pilot expansion tube using an unheated hydrogen driver," *Fourth Hypervelocity Techniques Symposium*. Tullahoma, Tennessee, 1965, pp. 7-26.

32.   Moore, J. A. "Description and initial operating performance of the Langley 6-inch expansion tube using heated helium driver gas." NASA-TM-X-3240, NASA Langley Research Center, Hampton, VA, 1975.

33.   Gildfind, D., Jacobs, P., Morgan, R., Chan, W., and Gollan, R. "Scramjet test flow reconstruction for a large-scale expansion tube, Part 1: quasi-one-dimensional modelling," *Shock Waves*, 2017, pp. 1-21.
       https://doi.org/10.1007/s00193-017-0785-x

34.   Mizuno, H., Sawada, K., and Sasoh, A. "Numerical analysis of carbon dioxide flowfield in expansion-tube," *8th AIAA/ASME Joint Thermophysics and Heat Transfer Conference*. AIAA Paper 2002-3221, June 2002.

https://doi.org/10.2514/6.2002-3221.

35. Nompelis, I., Candler, G., Holden, M., and Wadhams, T. "Numerical simulation of high-enthalpy experiments in the LENS X expansion tube facility," *42nd AIAA Aerospace Sciences Meeting and Exhibit*. AIAA Paper 2004-1000, January 2004.
https://doi.org/10.2514/6.2004-1000.

36. Abul-Huda, Y. M., and Gamba, M. "Flow characterization of a hypersonic expansion tube facility for supersonic combustion studies," *Journal of Propulsion and Power* Vol. 33, No. 6, 2017, pp. 1504-1519.
https://doi.org/10.2514/1.B36543

37. Holden, M. S., Wadhams, T. P., MacLean, M. G., and Dufrene, A. T. "Measurements of real gas effects on regions of laminar shock wave/boundary layer interaction in hypervelocity flows for "blind'code validation studies," *21st AIAA Computational Fluid Dynamics Conference*. AIAA Paper 2013-2837, June 2013.
https://doi.org/10.2514/6.2013-2837.

38. McGilvray, M., Austin, J., Sharma, M., Jacobs, P., and Morgan, R. "Diagnostic modelling of an expansion tube operating condition," *Shock Waves* Vol. 19, No. 1, 2009, pp. 59-66.
https://doi.org/10.1007/s00193-009-0187-9

39. Ray, J., Kieweg, S., Dinzl, D., Carnes, B., Weirs, V. G., Freno, B., Howard, M., Smith, T., Nompelis, I., and Candler, G. V. "Estimation of inflow uncertainties in laminar hypersonic double-cone experiments," *AIAA journal* Vol. 58, No. 10, 2020, pp. 4461-4474.
https://doi.org/10.2514/1.J059033

40. Sharma, M., Swantek, A., Flaherty, W., Austin, J., Doraiswamy, S., and Candler, G. V. "Experimental and numerical investigation of hypervelocity carbon dioxide flow over blunt bodies," *Journal of thermophysics and heat transfer* Vol. 24, No. 4, 2010, pp. 673-683.
https://doi.org/10.2514/1.49386

41. Toniato, P., Gildfind, D., Jacobs, P., and Morgan, R. "Expansion tube nozzle design using a parallel simplex algorithm," *Shock Waves* Vol. 30, No. 2, 2020, pp. 185-199.
https://doi.org/10.1007/s00193-019-00930-2

42. Chue, R., Bakos, R., Tsai, C.-Y., and Betti, A. "Design of a shock-free expansion tunnel nozzle in HYPULSE," *Shock Waves* Vol. 13, No. 4, 2003, pp. 261-270.
https://doi.org/10.1007/s00193-003-0215-0

43. Goodwin, D. G., Speth, R. L., Moffat, H. K., and Weber, B. W. *Cantera: An object-oriented software toolkit for chemical kinetics, thermodynamics, and transport processes*. https://www.cantera.org, 2021. Version 2.5.1.
doi:10.5281/zenodo.4527812

44. Colonna, G., and Capitelli, M. "The influence of atomic and molecular metastable states in high-enthalpy nozzle expansion nitrogen flows," *Journal of Physics D: Applied Physics* Vol. 34, No. 12, 2001, p. 1812.
https://doi.org/10.1088/0022-3727/34/12/308

45. Colonna, G., and Capitelli, M. "Self-consistent model of chemical, vibrational, electron kinetics in nozzle expansion," *Journal of thermophysics and heat transfer* Vol. 15, No. 3, 2001, pp. 308-316.
https://doi.org/10.2514/2.6627

46. Shizgal, B. D., and Lordet, F. "Vibrational nonequilibrium in a supersonic expansion with reaction: Application to O_2–O," *The Journal of chemical physics* Vol. 104, No. 10, 1996, pp. 3579-3597.
https://doi.org/10.1063/1.471062

47. Colonna, G., Tuttafesta, M., Capitelli, M., and Giordano, D. "Non-Arrhenius NO formation rate in one-dimensional nozzle airflow," *Journal of thermophysics and heat transfer* Vol. 13, No. 3, 1999, pp. 372-375.
https://doi.org/10.2514/2.6448

48. Hao, J., Wang, J., and Lee, C. "State-specific simulation of oxygen vibrational excitation and dissociation behind a normal shock," *Chemical Physics Letters* Vol. 681, 2017, pp. 69-74.
https://doi.org/10.1016/j.cplett.2017.05.042

49. Grover, M. S., Valentini, P., Josyula, E., and Chaudhry, R. S. "Vibrational state-to-state and multiquantum effects for N2+ N2 interactions at high temperatures for aerothermodynamic applications," *AIAA Scitech 2020 Forum*. AIAA Paper 2020-1227, January 2020.
https://doi.org/10.2514/6.2020-1227

50. Lopez, B., and Lino Da Silva, M. "Non-Boltzmann analysis of hypersonic air re-entry flows," *11th AIAA/ASME Joint Thermophysics and Heat Transfer Conference*. AIAA Paper 2014-2547, June 2014.
https://doi.org/10.2514/6.2014-2547

51. Lino da Silva, M., Loureiro, J., and Guerra, V. "A multiquantum dataset for vibrational excitation and dissociation in high-temperature O2–O2 collisions," *Chemical Physics Letters* Vol. 531, 2012, pp. 28-33.
https://doi.org/10.1016/j.cplett.2012.01.074

52. Lino da Silva, M., Guerra, V., and Loureiro, J. "State-resolved dissociation rates for extremely nonequilibrium atmospheric entries," *Journal of thermophysics and heat transfer* Vol. 21, No. 1, 2007, pp. 40-49.
https://doi.org/10.2514/1.24114

53. Gu, S., Hao, J., and Wen, C.-Y. "On the Vibrational State-Specific Modelling of Radiating Normal-Shocks in Air," *AIAA Journal* Vol. Articles in Advance, 2022.
https://doi.org/10.2514/1.J061438

54. Adamovich, I. V., Macheret, S. O., Rich, J. W., and Treanor, C. E. "Vibrational energy transfer rates using a forced harmonic oscillator model," *Journal of Thermophysics and Heat Transfer* Vol. 12, No. 1, 1998, pp. 57-65.
https://doi.org/10.2514/2.6302

55. Adamovich, I. V., Macheret, S. O., Rich, J. W., and Treanor, C. E. "Vibrational relaxation and dissociation behind shock waves. Part 1-Kinetic rate models," *AIAA journal* Vol. 33, No. 6, 1995, pp. 1064-1069.
https://doi.org/10.2514/3.12528

56. Lino da Silva, M., Lopez, B., Guerra, V., and Loureiro, J. "A multiquantum state-to-state model for the fundamental states of air: the stellar database," *Proceedings of 5th International Workshop on Radiation of High Temperature Gases in Atmospheric Entry*. Vol. 714, ESASP, Noordwijk, The Netherlands, 2012, p. 16.

57. Oblapenko, G. "Calculation of vibrational relaxation times using a kinetic theory approach," *The Journal of Physical Chemistry A* Vol. 122, No. 50, 2018, pp. 9615-9625.
https://doi.org/10.1021/acs.jpca.8b09897

58. Esposito, F., Armenise, I., and Capitelli, M. "N–N2 state to state vibrational-relaxation and dissociation rates based on quasiclassical calculations," *Chemical Physics* Vol. 331, No. 1, 2006, pp. 1-8.
https://doi.org/10.1016/j.chemphys.2006.09.035

59. Esposito, F., and Capitelli, M. "The relaxation of vibrationally excited O2 molecules by atomic oxygen," *Chemical physics letters* Vol. 443, No. 4-6, 2007, pp. 222-226.
https://doi.org/10.1016/j.cplett.2007.06.099

60. Su, W., Bruno, D., and Babou, Y. "State-specific modeling of vibrational relaxation and nitric oxide formation in shock-heated air," *Journal of Thermophysics and Heat Transfer* Vol. 32, No. 2, 2018, pp. 337-352.
https://doi.org/10.2514/1.T5271

61. Millikan, R. C., and White, D. R. "Systematics of vibrational relaxation," *The Journal of chemical physics* Vol. 39, No. 12, 1963, pp. 3209-3213.
https://doi.org/10.1063/1.1734182

62. Park, C. "Review of chemical-kinetic problems of future NASA missions. I-Earth entries," *Journal of Thermophysics and Heat transfer* Vol. 7, No. 3, 1993, pp. 385-398.
https://doi.org/10.2514/3.431

63. Bose, D., and Candler, G. V. "Thermal rate constants of the N2+ O→ NO+ N reaction using ab initio 3 A ″ and 3 A′ potential energy surfaces," *The Journal of chemical physics* Vol. 104, No. 8, 1996, pp. 2825-2833.
https://doi.org/10.1063/1.471106

64.   Bose, D., and Candler, G. V. "Thermal rate constants of the O2+ N$\rightarrow$ NO+ O reaction based on the A 2$'$ and A 4$'$ potential-energy surfaces," *The Journal of chemical physics* Vol. 107, No. 16, 1997, pp. 6136-6145. https://doi.org/10.1063/1.475132

65.   Andrienko, D. A., and Boyd, I. D. "State-specific dissociation in O2–O2 collisions by quasiclassical trajectory method," *Chemical Physics* Vol. 491, 2017, pp. 74-81. https://doi.org/10.1016/j.chemphys.2017.05.005

66.   Luo, H., Kulakhmetov, M., and Alexeenko, A. "Ab initio state-specific N2+ O dissociation and exchange modeling for molecular simulations," *The Journal of chemical physics* Vol. 146, No. 7, 2017, p. 074303. https://doi.org/10.1063/1.4975770

67.   Esposito, F., and Armenise, I. "Reactive, inelastic, and dissociation processes in collisions of atomic oxygen with molecular nitrogen," *The Journal of Physical Chemistry A* Vol. 121, No. 33, 2017, pp. 6211-6219. https://doi.org/10.1021/acs.jpca.7b04442

68.   Esposito, F., and Armenise, I. "Reactive, Inelastic, and Dissociation Processes in Collisions of Atomic Nitrogen with Molecular Oxygen," *The Journal of Physical Chemistry A* Vol. 125, No. 18, 2021, pp. 3953-3964. https://doi.org/10.1021/acs.jpca.0c09999

69.   Ozbenli, E., Vedula, P., Vogiatzis, K., and Josyula, E. "Numerical solution of hypersonic flows via artificial neural networks," *AIAA Scitech 2020 Forum*. AIAA Paper 2020-1233, January 2020. https://doi.org/10.2514/6.2020-1233

70.   Guy, A., Bourdon, A., and Perrin, M.-Y. "Consistent multi-internal-temperatures models for nonequilibrium nozzle flows," *Chemical Physics* Vol. 420, 2013, pp. 15-24. https://doi.org/10.1016/j.chemphys.2013.04.018

71.   Sahai, A., Johnston, C. O., Lopez, B., and Panesi, M. "Flow-radiation coupling in CO2 hypersonic wakes using reduced-order non-Boltzmann models," *Physical Review Fluids* Vol. 4, No. 9, 2019. https://doi.org/10.1103/PhysRevFluids.4.093401

72.   Munafo, A., Panesi, M., Jaffe, R., Colonna, G., Bourdon, A., and Magin, T. "QCT-based vibrational collisional models applied to nonequilibrium nozzle flows," *The European Physical Journal D* Vol. 66, No. 7, 2012, pp. 1-11. https://doi.org/10.1140/epjd/e2012-30079-3

73.   Bender, D. J., Mitchner, M., and Kruger, C. "Measurement of vibrational population distributions in a supersonic expansion of carbon monoxide," *The Physics of Fluids* Vol. 21, No. 7, 1978, pp. 1073-1085. https://doi.org/10.1063/1.862345

74.   Horn, K., and Oettinger, P. "Vibrational energy transfer in diatomic gas mixtures," *The Journal of Chemical Physics* Vol. 54, No. 7, 1971, pp. 3040-3046. https://doi.org/10.1063/1.1675290

75.   Aliat, A., Vedula, P., and Josyula, E. "Simple model for vibration-translation exchange at high temperatures: Effects of multiquantum transitions on the relaxation of a N2 gas flow behind a shock," *Physical Review E* Vol. 83, No. 2, 2011, p. 026308. https://doi.org/10.1103/PhysRevE.83.026308

76.   Lino da Silva, M., Passarinho, F., Alexandrova, T., and Dudeck, M. "Modelling of the Arc‐Jet Plasma Flow in the SR5 Nozzle Using a Thermochemical Nonequilibrium and a State‐to‐State Approach," *AIP Conference Proceedings*. Vol. 762, American Institute of Physics, 2005, pp. 1183-1188. https://doi.org/10.1063/1.1941695.

77.   Candler, G. V. "Nonequilibrium hypersonic flows and hypersonic nozzle flow modeling," *NATO STO Lecture Series: Flow Characterization and Modeling of Hypersonic Wind Tunnels*. STO-AVT-352-VKI, Von Kármán Institute for Fluid Dynamics, Sint-Genesius-Rode, Belgium, 2018.

78.   Olejniczak, J., and Candler, G. V. "Vibrational energy conservation with vibration–dissociation coupling: General theory and numerical studies," *Physics of Fluids* Vol. 7, No. 7, 1995, pp. 1764-1774. https://doi.org/10.1063/1.868491

79. Candler, G. V. "Rate effects in hypersonic flows," *Annual Review of Fluid Mechanics* Vol. 51, 2019, pp. 379-402. https://doi.org/10.1146/annurev-fluid-010518-040258

80. Anderson Jr, J. D. "A time-dependent analysis for vibrational and chemical nonequilibrium nozzle flows," *AIAA Journal* Vol. 8, No. 3, 1970, pp. 545-550. https://doi.org/10.2514/3.5703

81. Fangman, A. J., and Andrienko, D. "A state-to-state and multi-temperature study of air thermochemistry," *AIAA Scitech 2021 Forum*. AIAA Paper 2021-0316, January 2021. https://doi.org/10.2514/6.2021-0316

82. Hao, J., Wang, J., and Lee, C. "Assessment of vibration–dissociation coupling models for hypersonic nonequilibrium simulations," *Aerospace Science and Technology* Vol. 67, 2017, pp. 433-442. https://doi.org/10.1016/j.ast.2017.04.027

83. Hannemann, K., Karl, S., Schramm, J. M., and Steelant, J. "Methodology of a combined ground based testing and numerical modelling analysis of supersonic combustion flow paths," *Shock Waves* Vol. 20, No. 5, 2010, pp. 353-366. https://doi.org/10.1007/s00193-010-0269-8

84. Jacobs, P., Morgan, R., Brandis, A., Buttsworth, D., Dann, A., D'Souza, M., Eichmann, T., Gildfind, D., Gollan, R., and Jacobs, C. "Design, operation and testing in expansion tube facilities for super-orbital re-entry," *NATO STO Lecture Series: Radiation and Gas-Surface Interaction (GSI) Phenomena on High Speed Re-Entry*. AVT-218-VKI, von-Karman Inst., Sint-Genesius Rode, Belgium, 2013.

85. Strand, J. S., and Goldstein, D. B. "Global sensitivity analysis for DSMC simulations of hypersonic shocks," *Journal of Computational Physics* Vol. 246, 2013, pp. 184-206. https://doi.org/10.1016/j.jcp.2013.03.035

86. Gimelshein, S. F., and Wysong, I. J. "Validation of high-temperature air reaction and relaxation models using emission data," *Journal of Thermophysics and Heat Transfer* Vol. 33, No. 3, 2019, pp. 606-616. https://doi.org/10.2514/1.T5555

87. Lino da Silva, M. "SPARK Line-by-Line v.3.0 User Manual." Institute of Plasmas and Nuclear Fusion, Instituto Superior Técnico, Lisbon, 2021.

88. Cruden, B. A., and Brandis, A. M. "Measurement and prediction of radiative non-equilibrium for air shocks between 7-9 km/s," *47th AIAA Thermophysics Conference*. AIAA Paper 2017-4535, June 2017. https://doi.org/10.2514/6.2017-4535

89. Wen, C., and Hornung, H. "Nonequilibrium recombination after a curved shock wave," *Progress in Aerospace Sciences* Vol. 46, No. 2-3, 2010, pp. 132-139. https://doi.org/10.1016/j.paerosci.2009.11.001

90. Macrossan, M. N. "Hypervelocity flow of dissociating nitrogen downstream of a blunt nose," *Journal of Fluid Mechanics* Vol. 217, 1990, pp. 167-202. https://doi.org/10.1017/S0022112090000672

91. Hua, S., and Chih-Yung, W. "Theoretical investigation of shock stand-off distance for non-equilibrium flows over spheres," *Chinese Journal of Aeronautics* Vol. 31, No. 5, 2018, pp. 990-996. https://doi.org/10.1016/j.cja.2018.02.013

92. Belouaggadia, N., Olivier, H., and Brun, R. "Numerical and theoretical study of the shock stand-off distance in non-equilibrium flows," *Journal of Fluid Mechanics* Vol. 607, 2008, pp. 167-197. https://doi.org/10.1017/S0022112008001973

93. Chan, W. Y., Jacobs, P. A., Smart, M. K., Grieve, S., Craddock, C. S., and Doherty, L. J. "Aerodynamic design of nozzles with uniform outflow for hypervelocity ground-test facilities," *Journal of Propulsion and Power* Vol. 34, No. 6, 2018, pp. 1467-1478. https://doi.org/10.2514/1.B36938

94. Gildfind, D. E., Morgan, R. G., Jacobs, P. A., and McGilvray, M. "Production of high-Mach-number scramjet flow conditions in an expansion tube," *AIAA journal* Vol. 52, No. 1, 2014, pp. 162-177. https://doi.org/10.2514/1.J052383

95. James, C. M., Ravichandran, R., Smith, D. R., Cullen, T. G., and Morgan, R. "Scaled Apollo Capsule Heat Flux Measurements in the X3 Expansion Tube," *AIAA Aviation 2020 Forum*. AIAA Paper 2020-3278, January 2020. https://doi.org/10.2514/6.2020-3278.

96. Cullen, T., James, C., Gollan, R., and Morgan, R. "Development of a total enthalpy and Reynolds number matched Apollo re-entry condition in the X2 expansion tunnel," *31st International Symposium on Shock Waves 2*. Springer, Cham, Switzerland, 2017, pp. 197-204.

97. Shimamura, K., Okamoto, A., Fujiwara, Y., Higo, Y., Yamada, K., Komuro, T., and Tanno, H. "High-speed visualization for test-time evaluation of a JAXA HEK-X free-piston driven expansion tube," *AIAA SciTech 2019 Forum*. AIAA Paper 2019-1556, January 2019. https://doi.org/10.2514/6.2019-1556.

98. Sheikh, U. A., Morgan, R. G., and McIntyre, T. J. "Vacuum ultraviolet spectral measurements for superorbital earth entry in X2 expansion tube," *AIAA Journal* Vol. 53, No. 12, 2015, pp. 3589-3602. https://doi.org/10.2514/1.J054027

99. Fahy, E. J. "Superorbital re-entry shock layers: flight and laboratory comparisons," *Centre for Hypersonics, Dept. of Mechanical and Mining Engineering*. PhD Thesis, Univ. of Queensland, Brisbane, Queensland, Australia, 2017.

100. James, C. M., Lewis, S. W., Morgan, R. G., Liu, Y., and Lefevre, A. "Generating High-Speed Earth Reentry Test Conditions in an Expansion Tube," *Journal of Spacecraft and Rockets* Vol. 58, No. 2, 2021, pp. 345-362. https://doi.org/10.2514/1.A34821

101. Andrienko, D. A., and Boyd, I. D. "Kinetic models of oxygen thermochemistry based on quasi-classical trajectory analysis," *Journal of Thermophysics and Heat Transfer* Vol. 32, No. 4, 2018, pp. 904-916. https://doi.org/10.2514/1.T4968

102. Anderson, J. D. *Modern compressible flow: with historical perspective*. New York: McGraw-Hill New York, 2021.

103. Gollan, R. "Computational Modelling of High-Temperature Gas Effects with Application to Hypersonic Flows," *Centre for Hypersonics, Dept. of Mechanical and Mining Engineering*. PhD Thesis, Univ. of Queensland, Brisbane, Queensland, Australia, 2009.